BBA - Molecular Cell Research 1872 (2025) 119857

Contents lists available at ScienceDirect

BBA - Molecular Cell Research

journal homepage: www.elsevier.com/locate/bbamcr

CISD2 counteracts the inhibition of ER-mitochondrial calcium transfer by anti-apoptotic BCL-2

Jens Loncke [a,1], Ian de Ridder [a,1], Justin Kale [b], Larry Wagner [c], Allen Kaasik [d], Jan B. Parys [a], Martijn Kerkhofs [a,e], David W. Andrews [b], David Yule [c], Tim Vervliet [a,2], Geert Bultynck [a,*,2]

[a] KU Leuven, Laboratory for Molecular and Cellular Signaling, Department of Cellular and Molecular Medicine, Leuven Kanker Instituut, Campus Gasthuisberg O/N-1 B-802, Herestraat 49, BE-3000 Leuven, Belgium
[b] University of Toronto, Biological Sciences, Sunnybrook Research Institute, Toronto, ON M4N 3M5, Canada
[c] University of Rochester, Department of Pharmacology and Physiology, School of Medicine and Dentistry, 601 Elmwood Avenue, Box 711, Rochester, NY 14642, USA
[d] University of Tartu, Department of Pharmacology, Institute of Biomedicine and Translational Medicine, Tartu, Estonia
[e] Univ Lyon, Université Claude Bernard Lyon 1, CNRS, Inserm, Physiopathologie et Génétique du Neurone et du Muscle, UMR5261, U1315, Institut NeuroMyoGène, 69008 Lyon, France

ARTICLE INFO

Keywords:
IP_3 receptor
Iron-sulfur cluster proteins
Naf-1
BCL-2
Calcium signaling

ABSTRACT

CISD2, a 2Fe—2S cluster domain-containing protein, is implicated in Wolfram syndrome type 2, longevity and cancer. CISD2 is part of a ternary complex with IP_3 receptors (IP_3Rs) and anti-apoptotic BCL-2 proteins and enhances BCL-2's anti-autophagic function. Here, we examined how CISD2 impacted the function of BCL-2 in apoptosis and in controlling IP_3R-mediated Ca^{2+} signaling. Using purified proteins, we found a direct interaction between the cytosolic region of CISD2 and BCL-2's BH4 domain with a submicromolar affinity. At the functional level, the cytosolic region of CISD2, as a purified protein, did not affect the ability of BCL-2 to inhibit BAX-pore formation. In a cellular context, loss of CISD2 did not impede the suppression of apoptosis by BCL-2. Also, in Ca^{2+}-signaling assays, absence of CISD2 did not affect the inhibition of IP_3R-mediated Ca^{2+} release by BCL-2. Combined, these experiments indicate that CISD2 is not essential for BCL-2 function in apoptosis and cytosolic Ca^{2+} signaling. Instead, CISD2 overexpression enhanced BCL-2-mediated suppression of cytosolic IP_3R-mediated Ca^{2+} release. However, consistent with the presence of CISD2 and BCL-2 at mitochondria-associated ER membranes (MAMs), the most striking effect was observed at the level of ER-mitochondrial Ca^{2+} transfer. While BCL-2 overexpression inhibited ER-mitochondrial Ca^{2+} transfer, overexpression of CISD2 together with BCL-2 abrogated the effect of BCL-2. The underlying mechanism is linked to ER-mitochondrial contact sites, since BCL-2 reduced ER-mitochondrial contact sites while co-expression of CISD2 together with BCL-2 abolished this effect. These findings reveal a unique interplay between BCL-2 and CISD2 at Ca^{2+}-signaling nanodomains between ER and mitochondria.

1. Introduction

The B-cell lymphoma 2 (BCL-2) protein family controls cell survival by regulating the connected processes of mitochondrial outer membrane permeabilization (MOMP) and apoptosis [1–4]. MOMP can be exerted by pro-apoptotic effector BCL-2 family proteins, such as BCL-2-associated X protein (BAX), and BCL-2 homologous antagonist/killer (BAK). The two other distinct groups of BCL-2 family proteins include a second set of pro-apoptotic members the BCL-2 homology (BH)3-only activators/sensitizers and the anti-apoptotic members, including the founding member of the family BCL-2 itself. All proteins of the BCL-2 family are characterized by the presence of one or several BCL-2 homology (BH) domains. Anti-apoptotic BCL-2 family members contain four BH domains (BH4-BH3-BH1-BH2). The BH3, BH1 and BH2 domains structurally encompass a hydrophobic cleft, which directly sequesters pro-apoptotic BCL-2-family members, thereby counteracting MOMP [5].

Beyond this canonical role, BCL-2 also controls apoptosis through modulation of Ca^{2+} homeostasis and dynamics. Particularly, Ca^{2+}

* Corresponding author.
E-mail address: geert.bultynck@kuleuven.be (G. Bultynck).
[1] Shared first authors.
[2] Shared last authors.

https://doi.org/10.1016/j.bbamcr.2024.119857
Received 9 May 2024; Received in revised form 19 September 2024; Accepted 27 September 2024
Available online 4 October 2024

signals arising from the endoplasmic reticulum (ER) have been implicated in cell death and survival decision [6]. A key Ca^{2+}-transport system in this context is the ER-resident inositol 1,4,5-trisphosphate (IP_3) receptor (IP_3R) [7]. This intracellular Ca^{2+}-release channel mediates the flux of Ca^{2+} from the ER lumen into the cytosol as well as towards the mitochondria. The Ca^{2+} transfer from the ER into mitochondria occurs at ER-mitochondrial contact sites harboring IP_3Rs, VDAC1, and ternary partners such as the chaperone glucose regulated protein 75 (GRP75) [8,9]. Large ER-mitochondrial Ca^{2+} fluxes are deleterious for cell survival [10]. By directly interacting with the IP_3R via its BH4 domain, BCL-2 suppresses excessive Ca^{2+}-release through the channel as well as the resulting apoptosis [11]. Moreover, early research reported that ER-targeted BCL-2 can effectively reduce steady-state ER Ca^{2+} concentration, which can contribute to its anti-apoptotic effect [12].

Besides IP_3Rs, other BCL-2-interacting partners have emerged, including CDGSH iron-sulfur domain-containing protein 2 (CISD2; also known under the aliases of ERIS, Naf-1, Miner1, Noxp70 or WS2). Furthermore, CISD2 has been found to interact with IP_3Rs potentially forming a ternary complex [13]. CISD2 plays an important role in iron and ROS homeostasis ultimately promoting longevity and delaying ageing-related features [14–16]. Loss-of-function mutations in CISD2 are reported to cause Wolfram syndrome type 2 (WS2), a rare genetic disease that starts with diabetes mellitus at young age and further evolves towards severe neurological impacts. Additionally, CISD2 upregulation supports malignant features of several types of cancer cells [17–22].

CISD2 is anchored into the ER membrane via its transmembrane (TM) domain and was also identified as a MAM-resident protein [15,23,24]. Interestingly, CISD2 is also believed to alter Ca^{2+} dynamics within the MAMs though the exact impact remains poorly defined at the molecular level. Independent studies revealed an intricate link between CISD2 and BCL-2 [13,25,26]. CISD2 was found to directly interact with BCL-2 and was required for BCL-2 to inhibit BECLIN 1-mediated autophagy [13,27]. CISD2 may also be involved in BCL-2's control over ER luminal Ca^{2+} stores, since absence of CISD2 in H1299 cells abrogated the decrease in steady-state ER Ca^{2+} concentration evoked by BCL-2 overexpression [13]. Of note, another study reported decreased ER Ca^{2+} levels in CISD2-deficient mouse myoblasts, cells characterized by high endogenous BCL-2 expression levels [27]. Independently, it was revealed that CISD2 can target both the BH4 and the BH3 domain of BCL-2 [26]. Combined, these studies suggest that CISD2 is a direct interactor and regulator of BCL-2 and a functional co-factor at the ER that may directly or indirectly impact IP_3R function.

In this study, we set out to characterize the interplay between BCL-2, CISD2 and IP_3Rs and the functional impact thereof. Our work indicates that CISD2 directly binds to BCL-2 by targeting the BH4 domain. While CISD2 only modestly affected IP_3R-mediated Ca^{2+}-release in the cytosol and its inhibition by BCL-2, CISD2 had profound effects on the impact of BCL-2 at the ER-mitochondrial contact sites. BCL-2 overexpression limited ER-mitochondrial Ca^{2+} transfer, while CISD2 overexpression completely alleviated the suppression of ER-mitochondrial Ca^{2+} transfers by BCL-2. These effects may in part be due to remodeling of ER-mitochondrial contact sites that were reduced upon BCL-2 overexpression, a feature counteracted by overexpression of CISD2.

2. Results

2.1. CISD2 interacts with BCL-2 involving its BH4 domain

We studied the direct interaction between the cytosolic regions of CISD2, lacking its N-terminal and TM domain ($CISD2^{CYT}$), and BCL-2, lacking its TM domain ($BCL\text{-}2^{\Delta TM}$), as 6xHis-tagged proteins. Fig. 1A displays schematic representations of the CISD2 and BCL-2 proteins, their relevant domains and the fragments used for the interaction analysis. These proteins were purified from *E. coli* using gravity-flow chromatography over Ni-NTA beads [28,29] and their quality and identity was validated using sodium dodecyl sulfate polyacrylamide gel electrophoresis (SDS-PAGE), general protein staining, and immunoblotting (Supplementary Fig. 1). To evaluate a direct interaction between CISD2 and BCL-2, co-immunoprecipitation experiments were set

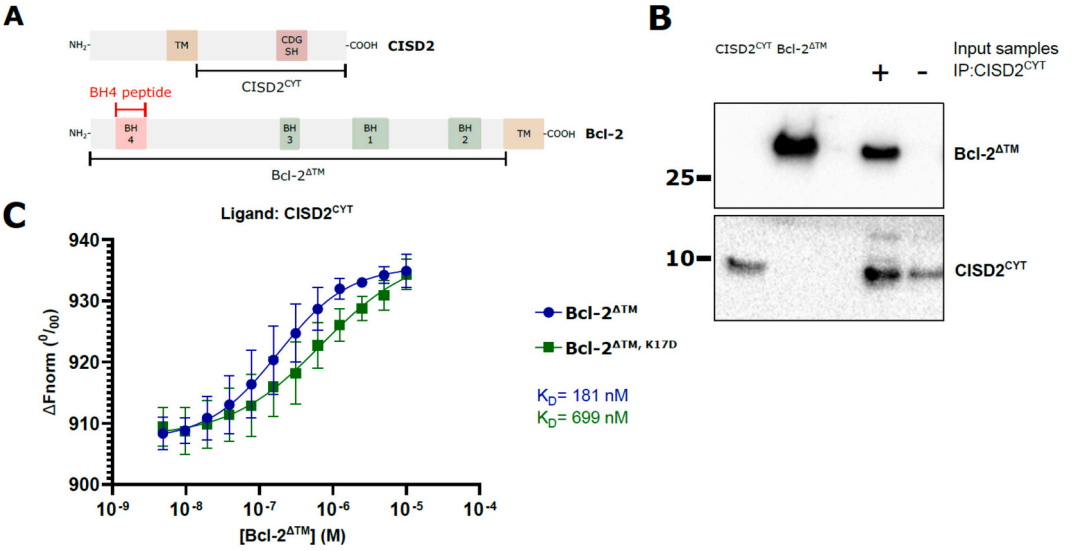

Fig. 1. BCL-2 and CISD2 are high affinity, direct interactors. A: Protein structure of CISD2 (top) and BCL-2 (bottom). Protein length and domain sizes are drawn to scale. Black lines indicate purified cytosolic fragments. The red line indicates the BH4 peptide that was used in biolayer interferometry (BLI) experiments. TM: transmembrane domain, CGSH: iron-sulfur cluster binding domain, BH: BCL-2 homology domain. B: Immunoblot of co-immunoprecipitation experiment using purified 6xHis-tagged C-terminal part of CISD2 ($CISD2^{CYT}$) and 6xHis-tagged $BCL\text{-}2^{\Delta TM}$. 6xHis-$CISD2^{CYT}$ was immunoprecipitated using an anti-CISD2 antibody. The immunoblot shown is a representative blot out of three biological replicates ($N = 3$). Molecular weight of the protein standards are indicated in kDa. C: Binding curves showing the interaction of purified and RED-tris-NTA labeled 6xHis-$CISD2^{CYT}$ with various concentrations of 6xHis-$BCL\text{-}2^{\Delta TM}$ (blue) and 6xHis-$BCL\text{-}2^{\Delta TM,\ K17D}$ (green) generated by through MicroScale Thermophoresis. On the y-axis the ratio of normalized fluorescence (ΔF_{norm}) is presented while the x-axis presents a logarithmic scale of the respective ligand concentration. Each data point represents the mean and error bars show the standard error of mean from N = 3 biological replicates, each with two technical measurements. (For interpretation of the references to colour in this figure legend, the reader is referred to the web version of this article.)

up (Fig. 1B). Purified CISD2^{CYT} and BCL-2$^{\Delta TM}$ were incubated and CISD2^{CYT} was immunoprecipitated using an anti-CISD2 antibody. Analysis of immunoprecipitation samples by SDS-PAGE and subsequent immunoblotting indicated that BCL-2$^{\Delta TM}$ co-immunoprecipitated with CISD2^{CYT}. In order to study the direct interaction between CISD2^{CYT} to BCL-2$^{\Delta TM}$ in a quantitative manner, microscale thermophoresis (MST) experiments were performed. CISD2^{CYT} was fluorescently labeled and its mobility within the thermophoretic gradient was monitored in the presence of different concentrations of BCL-2$^{\Delta TM}$ (Fig. 1C). Correlating with the immunoprecipitation experiments, we observed an interaction between CISD2^{CYT} and BCL-2$^{\Delta TM}$ with a dissociation constant (K_D) value of 0.2 μM (Fig. 1C). Subsequently, we purified mutant BCL-2$^{\Delta TM,\ K17D}$ harboring a mutation in the BH4 domain, which impairs binding to the IP_3R [30], and evaluated the effect of this mutation on the interaction with CISD2^{CYT} using MST (Fig. 1C). Although BCL-2$^{\Delta TM,\ K17D}$ bound CISD2^{CYT}, with a binding affinity of 0.7 μM, which is approximately 3.5-fold lower compared to BCL-2$^{\Delta TM}$. This result suggested that the cytosolic regions of CISD2 and BCL-2 directly interact at least in part through the BH4 domain of BCL-2.

2.2. The BH4 domain of BCL-2 contributes to the interaction with CISD2

Next, we aimed to examine the binding of CISD2^{CYT} to BCL-2's BH4 domain using biolayer interferometry (BLI), which is a reliable technique to study the binding kinetics of peptide-protein interactions. First, to verify our findings of the MST analysis we evaluated the binding of CISD2^{CYT} and BCL-2$^{\Delta TM}$ by immobilizing BCL-2$^{\Delta TM}$ on BLI Octet® Amine Reactive 2nd Generation (AR2G) biosensors via amide coupling and observed a K_D of approximately 1 μM (Fig. 2A). Subsequently, we immobilized biotinylated BH4^{BCL-2} peptides to streptavidin-coated BLI biosensors and evaluated their binding kinetics with various concentrations of CISD2^{CYT} (Supplementary Fig. 2A). To ensure the specificity of the interaction, we also assessed the interaction between CISD2^{CYT} with two scrambled versions of the BH4^{BCL-2} peptide (BH4^{scr1} and BH4^{scr2}) (Supplementary Fig. 2B and 2C) and used their combined averages as non-specific binding references to correct our data on the interaction with the BH4^{BCL-2} peptide (Fig. 2B). We found a scrambled-corrected K_D of 910 nM for purified CISD2^{CYT} binding to the BH4^{BCL-2} peptide (Fig. 2C). We validated the specificity of CISD2^{CYT} binding to BH4^{BCL-2} by evaluating the inherent adsorption of the peptide using an unrelated protein, namely bovine serum albumin (BSA). No interaction between BSA and the BH4^{BCL-2} peptide was observed (Supplementary Fig. 2D). Altogether, using multiple techniques for in vitro interaction analysis, we observed that CISD2^{CYT} directly interacts with BCL-2$^{\Delta TM}$, at least in part via its BH4 domain in the submicromolar K_D range. The similar K_D values observed in our BLI experiments between CISD2^{CYT} and Bcl-2$^{\Delta TM}$ on the one hand, and CISD2^{CYT} and the BH4^{BCL-2} peptide on the other hand might suggest that the BH4 domain is the main region of BCL-2 binding to CISD2. However, since we used the cytosolic fragments of both proteins, we cannot exclude the contribution of the TM domain of BCL-2 and the N-terminal and TM domains of CISD2 to the interaction of the full-length BCL-2 and CISD2 proteins.

2.3. CISD2 does not affect BCL-2's anti-apoptotic function

Given the important anti-apoptotic role of BCL-2 in suppressing BAX/BAK-mediated MOMP [1,31] but also in the prevention of IP_3R-dependent mitochondrial Ca^{2+} overload mediated MOMP [5,32,33], we aimed to assess whether CISD2 can impact the anti-apoptotic properties of BCL-2. First, we studied the role of CISD2 on the 'canonical' anti-

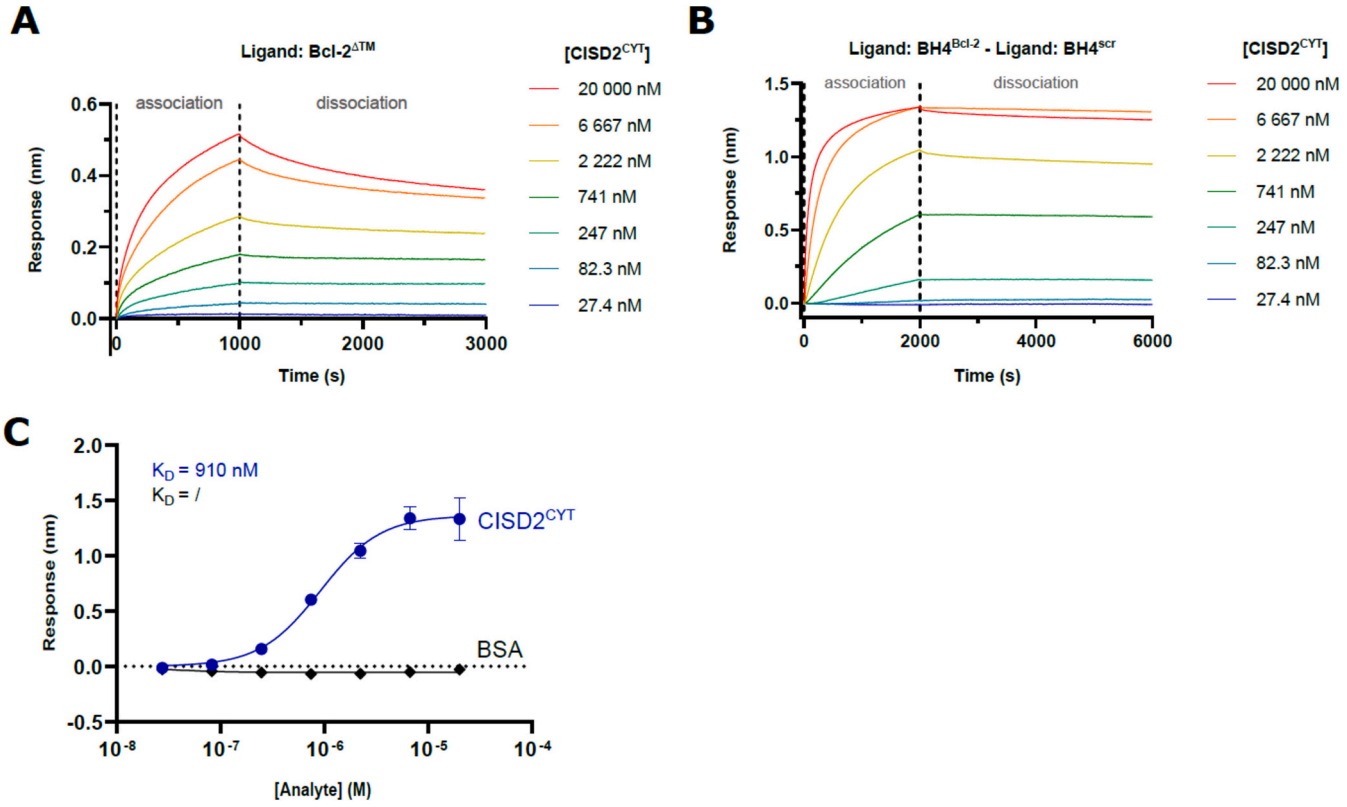

Fig. 2. CISD2 binds to BCL-2 via its BH4 domain. A: Real-time BLI curves of 6xHis-CISD2^{CYT} to 6xHis-BCL-2$^{\Delta TM}$ immobilized on AR2G biosensors (N = 3) B: Real-time BLI curves of 6xHis-CISD2^{CYT} to immobilized biotin-BH4^{BCL-2}, referenced using the BLI curves of two scrambled biotin-BH4 peptides (BH4^{scr}) as non-specific binding references. C: Steady state binding analysis of data shown in B highlighting specificity of binding. Binding to the two scrambled biotin-BH4^{BCL-2} peptides were used as non-specific binding references to correct the results obtained with biotin-BH4^{BCL-2} (BH4^{BCL-2} - BH4^{scr}) on top of the original naked sensor references. Means of respectively N = 3 (BH4^{BCL-2}) or *N* = 5 (BH4^{scr}) biological replicates were evaluated. Error bars indicate standard error of the mean.

apoptotic role of BCL-2, i.e. counteracting BAX-mediated pore formation. Capitalizing on the access to purified BCL-$2^{\Delta TM}$ and $CISD2^{CYT}$ proteins, we performed a second mitochondria-derived activator of caspases (SMAC)-mCherry release assay using permeabilized baby mouse kidney (BMK) BAX/BAK double knock-out (DKO) cells. In this setup, BAX-pore formation and MOMP is induced and monitored through the addition of purified BAX, caspase-8-cleaved Bid (cBID) and/or the proteins of interest. In the absence of cBID, the SMAC-mCherry is localized in the mitochondria in live cells and the mitochondrial SMAC-mCherry signal remained stable, as shown in the first columns of Fig. 3A and B, indicating that BAX is not spontaneously activated. Upon addition of the activating BH3-only protein cBID, BAX is activated, thereby resulting in BAX-pore formation and subsequent MOMP, leading to a decrease of fluorescence of SMAC-mCherry in the mitochondria, as observed in the second columns of Fig. 3A and B. Upon addition of varying concentrations of purified BCL-$2^{\Delta TM}$ (from 0.0001 nM to 1 μM), cBID-induced BAX-mediated MOMP was prevented, whereby SMAC-mCherry localization was retained in the mitochondria (third column

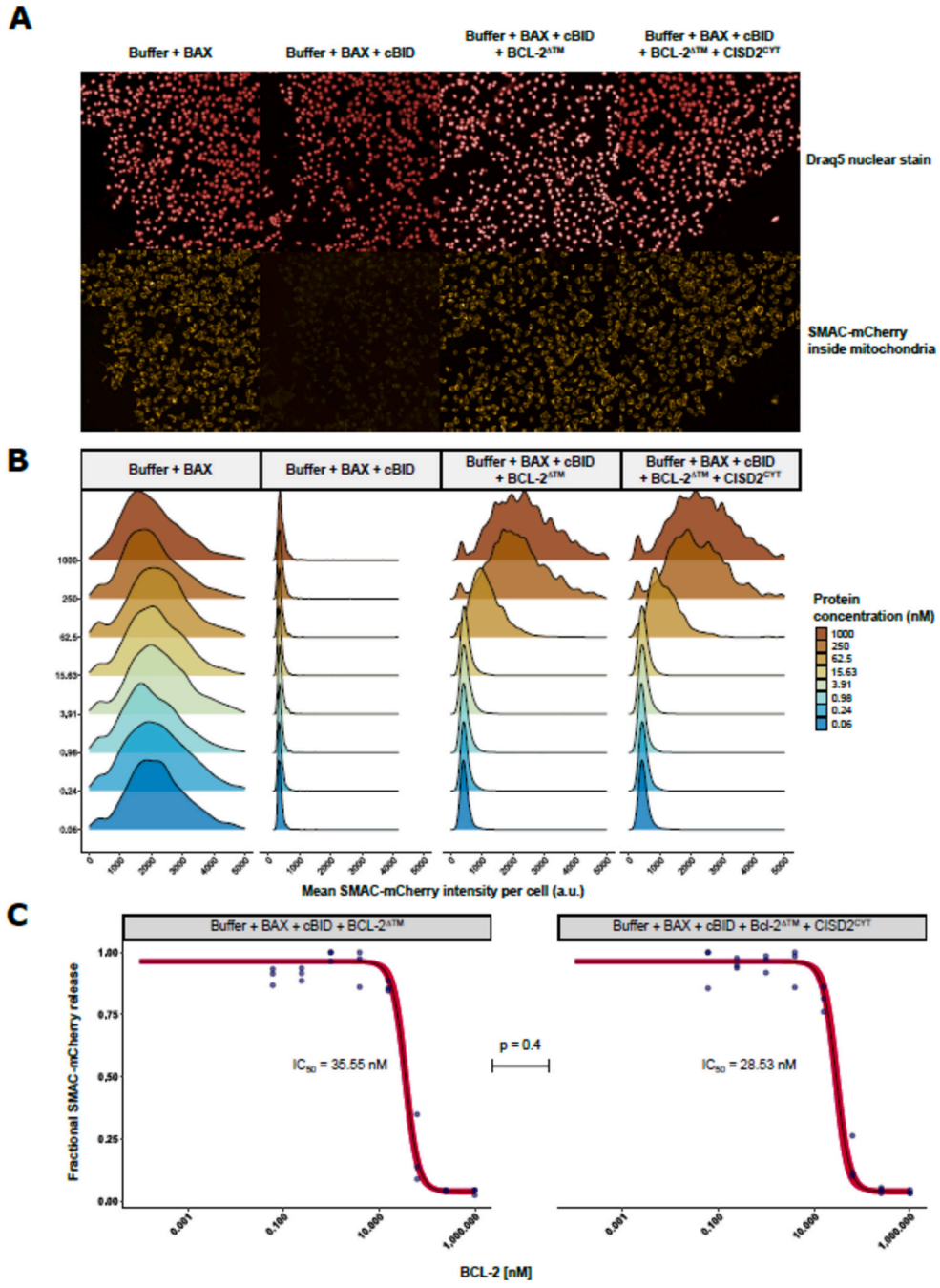

Fig. 3. CISD2 does not affect BCL-2's potency to prevent BAX-mediated mitochondrial outer membrane permeabilization. A: Representative microscopic acquisitions of DRAQ5 and SMAC-mCherry fluorescence in permeabilized baby mouse kidney (BMK) BAX/BAK double knock-out (DKO) cells. B: Kernel density estimate of mean SMAC-mCherry intensity per cell for different protein concentrations of a single representative replicate. a.u.: arbitrary units. C: IC_{50} (half-maximal inhibitory concentration)-fit curves of fractional Smac-mCherry release for BMK BAX/BAK DKO cells with added purified BAX, cBID and BCL-$2^{\Delta TM}$ in presence and absence of 2 μM $CISD2^{CYT}$. Black line corresponds to averages of N = 3 experiments. Red shade corresponds to 95 % confidence interval of fit. Blue shaded data points indicate individual replicates. (Wilcoxon rank sum exact test W = 2, $p = 0.4$). (For interpretation of the references to colour in this figure legend, the reader is referred to the web version of this article.)

of Fig. 3A and B). The half-effective inhibitory concentration (IC_{50}) for the inhibition of BAX-pore formation by BCL-$2^{\Delta TM}$ was determined to be 36 nM (Fig. 3C). Next, we asked whether addition of excess $CISD2^{CYT}$ (2 μM) could impact BCL-$2^{\Delta TM}$ prevention of BAX-pore formation. However, addition of 2 μM $CISD2^{CYT}$ did not impede BCL-2 suppression of BAX-pore formation (fourth column of Fig. 3A and B). The IC_{50} for the inhibition of Bax-pore formation by BCL-$2^{\Delta TM}$ in the presence of $CISD2^{CYT}$ was 29 nM (Fig. 3C), suggesting that CISD2 did not affect BCL-2's canonical anti-apoptotic function.

2.4. Bcl-2 does not rely on CISD2 to exert its anti-apoptotic role

Since BCL-2 also counteracts apoptosis in part through preventing mitochondrial Ca^{2+} overload, we assessed whether CISD2 is needed for this anti-apoptotic effect. To this end, we generated CISD2 KO HeLa cells via CRISPR/Cas9, and Cas9 control cells and exposed them to staurosporine (STS), an apoptotic agent that acts via mitochondrial Ca^{2+} overload [29]. HeLa Cas9 control and CISD2 KO cells were subjected to 500 nM STS treatment for 6 h, in the presence and absence of BCL-2 overexpression. Apoptosis was monitored by detecting poly (ADP-ribose) polymerase (PARP) levels via immunoblotting. Evaluation of PARP cleavage, by quantifying cleaved PARP over total PARP levels, is a ratiometric measure to reliably detect apoptosis [34]. A representative immunoblot is shown in Fig. 4A. Densitometric quantification of PARP cleavage is shown in Fig. 4B. STS (500 nM) similarly increased PARP cleavage in HeLa Cas9 control and CISD2 KO cells, showing that absence of CISD2 does not affect the susceptibility of cells towards apoptotic stimuli. Moreover, in the absence of STS, no PARP cleaving was observed in either HeLa Cas9 control and CISD2 KO cells. Furthermore, BCL-2 overexpression evoked a protective effect and decreased PARP cleavage in both HeLa Cas9 control and CISD2 KO cells.

2.5. CISD2 is not required for BCL-2 to bind to and inhibit IP_3Rs

Beyond the canonical anti-apoptotic function of BCL-2, it is well established that BCL-2 can also impact Ca^{2+} dynamics by directly targeting the IP_3R. The inhibition of IP_3R-mediated Ca^{2+} flux by BCL-2 is mediated by the BH4 domain of BCL-2 [11]. Furthermore, the present study as well as work by others [13,25,26] indicate that CISD2 directly interacts with BCL-2 via its BH4 domain, opening up the possibility that CISD2 is a modulator of BCL-2 functions that involve its BH4 domain. Therefore, we evaluated the possibility that CISD2 is involved in the modulation of IP_3Rs by BCL-2. First, we evaluated whether BCL-2 relies on CISD2 to interact with IP_3R1, the most important IP_3R isoform in HeLa cells [35]. We transfected a triple FLAG-tagged (3xFLAG-) BCL-2 or the empty vector control in HeLa Cas9 control and CISD2 KO cells. By immunoprecipitating 3xFLAG-BCL-2 we observed co-immunoprecipitation of endogenous IP_3R1 (Fig. 5A). We found no significant difference in co-immunoprecipitated IP_3R1 levels relative to pulled down 3xFLAG-BCL-2 in HeLa Cas9 control and CISD2 KO cells (Fig. 5B). This indicates that although CISD2 directly interacts with BCL-2, CISD2 is not essential for BCL-2 binding to IP_3R1. Next, we examined whether CISD2 was important for IP_3R inhibition by BCL-2 in living cells. To evaluate whether CISD2 could modulate BCL-2's inhibition of IP_3R-mediated Ca^{2+} release, we overexpressed 3xFLAG-BCL-2-p2a-mCherry, or expressed control empty vector p2a-mCherry in HeLa Cas9 control cells and HeLa CISD2 KO cells and measured IP_3R-mediated Ca^{2+} release into the cytosol using the ratiometric Ca^{2+} indicator Fura-2. Fig. 5C shows averaged traces of cytosolic Ca^{2+} signals in response to ATP (2 μM). The integrated cytosolic Ca^{2+} signal (area under the curve, AUC) was quantified. BCL-2 overexpression was found to significantly inhibit IP_3R-mediated Ca^{2+} release in both HeLa Cas9 control and HeLa CISD2 KO cells (Fig. 5D). There was no significant difference between Cas9 control and CISD2 KO cells overexpressing BCL-2. In addition, the percentage of responding cells revealed similar outcomes, with BCL-2 lowering the percentage of responding cells in both HeLa Cas9 control and HeLa CISD2 KO cells (Fig. 5E). These findings indicate that while CISD2 can directly interact with BCL-2, CISD2 is not essential for the interaction between BCL-2 and the IP_3R as well as for BCL-2 inhibition of IP_3R function. The data therefore advocates that BCL-2 directly interacts with and inhibits IP_3Rs, and not indirectly via CISD2.

2.6. CISD2 modestly enhances BCL-2 suppression of IP_3R-mediated cytosolic Ca^{2+} release in a cellular context

Although CISD2 is not essential for BCL-2 inhibition of IP_3R-mediated Ca^{2+} release, CISD2 may still modulate BCL-2's impact on IP_3R function. Particularly, the overexpression of BCL-2 may provide excess BCL-2 proteins in comparison to the endogenously available CISD2 proteins, thus limiting the ability to observe a modulatory effect. Moreover, since IP_3Rs and CISD2 appear to bind to BCL-2 via its BH4 domain, CISD2 may potentially compete with IP_3Rs for BCL-2 and thus potentially antagonize BCL-2's IP3R-inhibitory properties. We therefore overexpressed BCL-2 together with CISD2 in HeLa cells. Cells were transfected with 3xFLAG-p2a-mCherry +/− 3xFLAG-CISD2 or 3xFLAG-BCL-2-p2a-mCherry +/− 3xFLAG-CISD2. Only mCherry-positive cells were analyzed. BCL-2 overexpression significantly inhibited IP_3R-mediated Ca^{2+} release in HeLa cells, evoked by 2 μM ATP both in absence or presence of CISD2 overexpression (Fig. 5F and G). Analyzing the AUC of the ATP-induced Ca^{2+} release in the BCL-2-overexpressing cells, no significant difference between empty vector transfected and CISD2-overexpressing cells was observed. Yet, CISD2 overexpression together with BCL-2 significantly decreased the percentage of responding cells compared to BCL-2-overexpression alone (Fig. 5H). This

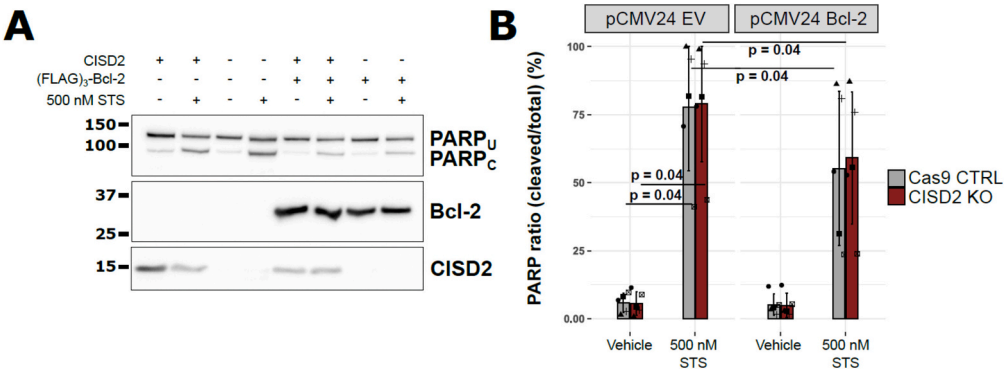

Fig. 4. Anti-apoptotic properties of BCL-2 are independent of CISD2. A: Immunoblot of a staurosporine-induced cell death experiment in HeLa Cas9 control and CISD2 KO cells, in presence and absence of BCL-2 overexpression. Molecular weights in kilodaltons are indicated with black bars. $PARP_u$: uncleaved PARP, $PARP_C$: cleaved PARP. B: Quantification of N = 5 immunoblots of cell death experiments, as shown in A. Error bars indicate standard deviations. STS: staurosporine. (Kruskal Wallis test: $\chi^2 = 30.208$, $p = 8.698e\text{-}05$).

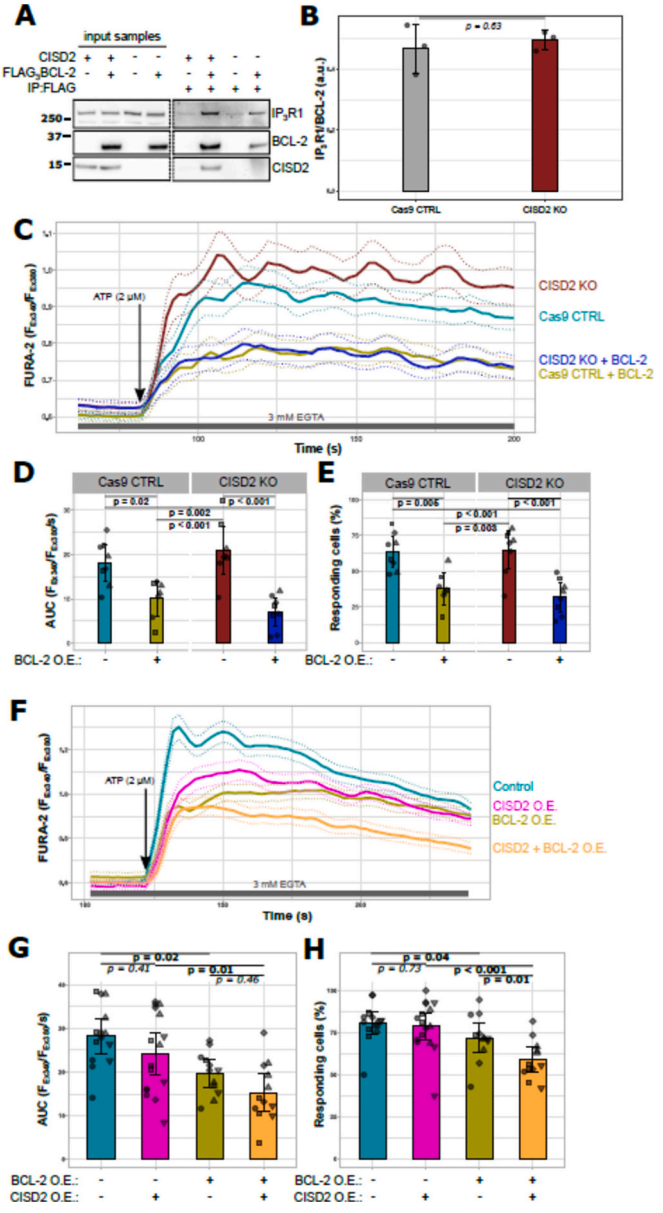

(caption on next column)

Fig. 5. CISD2 is not essential for binding of BCL-2 to IP_3R1, nor for BCL-2's capacity to inhibit IP_3R-mediated Ca^{2+} release. A: Immunoblot of co-immunoprecipitation experiment where overexpressed 3xFLAG-BCL-2 was pulled down with an anti-FLAG antibody, in presence or absence of endogenous CISD2. The shown immunoblot is a representative blot out of three biological replicates (N = 3). Molecular weights of the protein standards are indicated in kDa. B: Densitometric quantification of IP_3R that co-immunoprecipitated with 3xFLAG-BCL-2 in N = 3 experiments shown in A. Error bars indicate standard deviations. a.u.: arbitrary units. (Welch two sample *t*-test: $t = -0.54631$, $p = 0.6283$). C: Averaged traces of FURA-2 ratio over time of HeLa Cas9 control and HeLa CISD2 KO (CISD2 KO) cells, transfected with either pCMV24-p2a-mCherry or pCMV24-3xFLAG-BCL-2-p2a-mCherry. Dotted lines indicate 95 % CI. Black arrows indicate timepoint of stimulation with 2 µM ATP. Grey band indicates presence of 3 mM EGTA. F_{Ex340}: FURA-2 emission intensity at excitation wavelength 340 nm. F_{Ex380}: FURA-2 emission intensity at excitation wavelength 380 nm. ($N = 8$) D: Quantification of area under curve (AUC) of 2 µM ATP responses shown in C. Different point shapes correspond to date of acquisition. O.E.: overexpression. (Two-way ANOVA – BCL-2 expression: F = 37.3141, $p = 1.59e\text{-}06$). E: Quantification of percentage of responding cells to 2 µM ATP shown in C. Different point shapes correspond to different acquisition days (Two-way ANOVA – BCL-2 expression: F = 36.5974, $p = 1.857e\text{-}06$). F: Averaged traces of FURA-2 ratio over time of HeLa cells, overexpressing either pCMV24-p2a-mCherry or pCMV24-BCL-2-p2a-mCherry with or without co-overexpression of pCMV26-CISD2, or transfected pCMV26 empty vector. Dotted lines indicate 95 % CI. Black arrows indicate timepoint of stimulation with 2 µM ATP. Grey band indicates presence of 3 mM EGTA. Experiments were performed at least 12 times per condition. G: Quantification of area under curve (AUC) of cytosolic 2 µM ATP responses shown in F. Different point shapes correspond to date of acquisition. Each data point represents the mean value of the responses of all cells measured in 1 well. (Two-way ANOVA – BCL-2 expression: F = 18.8195, $p = 6.97e\text{-}05$) H: Quantification of percentage of responding cells to 2 µM ATP shown in F. Different point shapes correspond to different days of acquisition. (Kruskal-Wallis test: $\chi^2 = 12.86$, $p = 3.356e\text{-}04$).

outcome suggested that CISD2 can enhance the inhibition of IP_3Rs by BCL-2. Therefore, we also studied the direct impact of purified BCL-$2^{\Delta TM}$ and $CISD2^{CYT}$ on IP_3R1 single-channel activity using a nuclear patch-clamp technique in DT40 cells lacking endogenous IP_3Rs (IP_3R-3KO) cells in which rat IP_3R1 is overexpressed (Supplementary Fig. 3 A & B). Here, channel opening was triggered by 1 µM IP_3. In line with previous findings, purified BCL-$2^{\Delta TM}$ decreased the open probability of single IP_3R1 channels [28]. However, $CISD2^{CYT}$ neither directly suppressed IP_3R1 channel opening nor affected the potency of BCL-$2^{\Delta TM}$ to inhibit IP_3R-channel opening. Hence, our combined findings indicated that CISD2 does not antagonize BCL-2's inhibitory impact on IP_3Rs, yet in a cellular context CISD2 overexpression can modestly potentiate BCL-2-mediated inhibition of IP_3R-mediated Ca^{2+} from the ER to the cytosol.

2.7. CISD2 counteracts BCL-2-dependent inhibition of IP_3R-mediated Ca^{2+} transfer to the mitochondria

CISD2 and BCL-2 have been proposed to reside at the MAMs [24,36]. First, using biochemical MAM isolation, we validated that indeed CISD2 and BCL-2 are present in the MAMs in HeLa cells (Fig. 6A). Moreover, we also analyzed CISD2-KO cells and found BCL-2 is still present at the MAMs, indicating that CISD2 is not needed for BCL-2's presence at the MAMs. Next, we explored the possibility that CISD2 could affect the influence of BCL-2 on ER-mitochondria Ca^{2+} transfer, evoked by agonist-induced IP_3R-mediated Ca^{2+} release. Therefore, we employed the genetically encoded Ca^{2+} indicator G-CEPIA2mt, which localizes to the mitochondrial matrix [37]. Cells were co-transfected with G-CEPIA2mt and 3xFLAG-p2a-mCherry +/− 3xFLAG-CISD2 or 3xFLAG-BCL-2-p2a-mCherry +/− 3xFLAG-CISD2. Only mCherry-positive cells were analyzed. Overexpression of 3xFLAG-BCL-2 (with p2a-mCherry) and 3xFLAG-CISD2 was verified via immunoblotting. A representative blot is shown in Fig. 6B, indicating that BCL-2-protein levels are not decreased by overexpressing CISD2. G-CEPIA2mt signals were measured in mCherry-positive cells in response to ATP. Similar to our observations

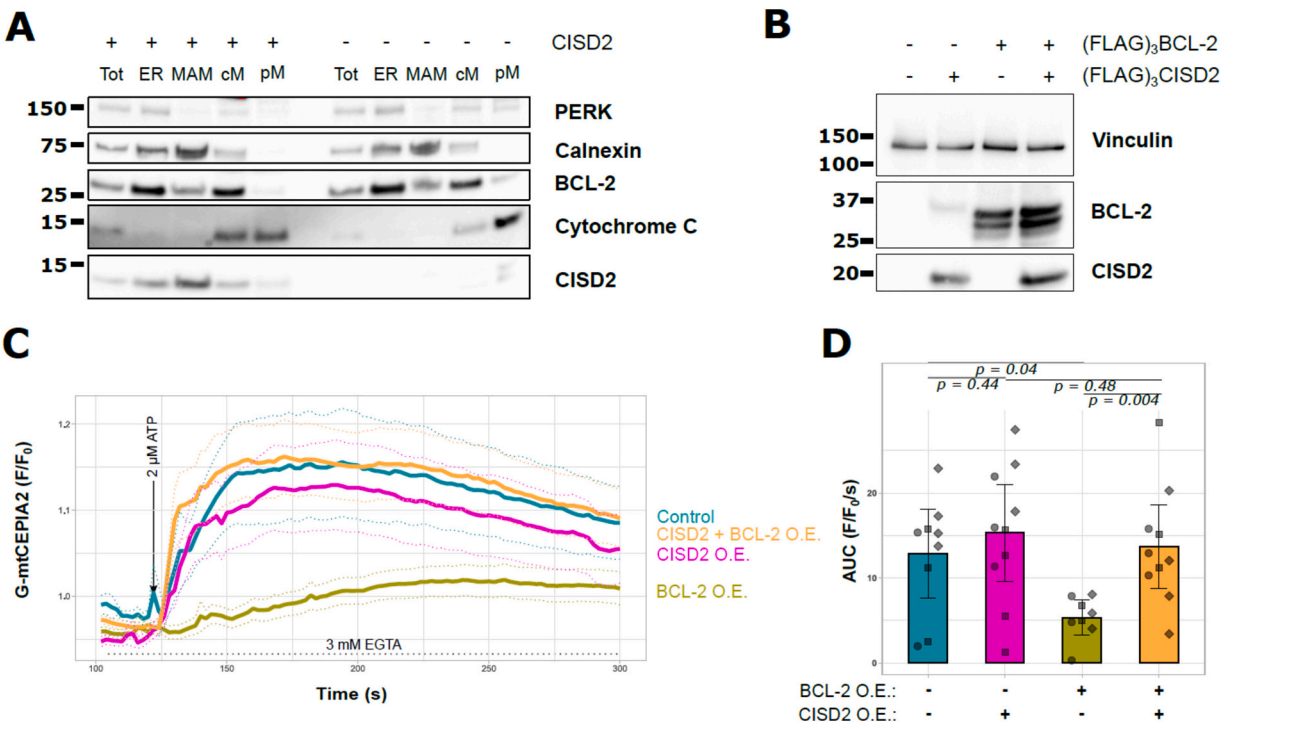

Fig. 6. Co-overexpression of CISD2 with BCL-2 abrogates inhibition by BCL-2 of IP_3R-mediated ER-mitochondrial Ca^{2+} transfer. A: Immunoblot of a typical subcellular fractionation experiment of HeLa Cas9 control and HeLa CISD2 KO cells. Molecular weights in kilodaltons are indicated with black bars. Tot: total protein lysate, ER: endoplasmic reticulum fraction, MAM: mitochondria-associated ER membrane fraction, cM: crude mitochondrial fraction, pM: pure mitochondrial fraction, PERK: Protein Kinase RNA-Like ER Kinase. B: Immunoblot of HeLa cells overexpressing 3xFLAG-BCL-2-p2a-mCherry or p2a-mCherry and 3xFLAG-CISD2 or transfected with pCMV26 empty vector. Molecular weights of the protein standards are indicated in kilodaltons are indicated. C: Averaged traces of normalized fluorescence of G-mtCEPIA2 (F/F_0) over time measured in HeLa cells, transfected with either pCMV24-p2a-mCherry or pCMV24-BCL-2-p2a-mCherry with or without co-overexpression of pCMV26-CISD2, or transfected pCMV26 empty vector. Dotted lines indicate 95 % CI. Black arrows indicate time point of stimulation with 2 µM ATP. Grey band indicates presence of 3 mM EGTA throughout the experiment. Experiments were performed at least 8 times per condition. D: Quantification of area under curve (AUC) of 2 µM ATP responses as measured in the mitochondria shown in C. Different point shapes correspond to date of acquisition. Each data point represents the mean value of the responses of all cells measured in 1 well. (Two-way ANOVA – BCL-2 expression: $F = 6.0279$, $p = 0.01952$).

of the cytosolic ATP-induced Ca^{2+} responses, overexpression of BCL-2 significantly inhibited ATP-evoked Ca^{2+} transfer from ER to mitochondria (Fig. 6C for averaged Ca^{2+} traces and Fig. 6D for quantification of Area Under Curve, $p = 0.04$). The inhibitory effect of BCL-2 on ER-mitochondrial Ca^{2+} transfers was completely abolished upon co-overexpression of CISD2 (Fig. 6C and D). CISD2 overexpression by itself had no effect on ER-mitochondria Ca^{2+} transfer (Fig. 6C and D). In conclusion, our results indicate that BCL-2 overexpression effectively abolishes ER-mitochondrial Ca^{2+} transfer. While CISD2 overexpression alone did not increase ER-mitochondria Ca^{2+} transfer, CISD2 was able to overrule BCL-2's inhibitory role.

2.8. BCL-2 impairs ER-mitochondrial contacts, while co-expression of CISD2 antagonizes this effect of BCL-2

In search of a mechanistic explanation as to why CISD2 is able to overcome BCL-2-mediated inhibition of ER-mitochondria Ca^{2+} transfer, we evaluated ER-mitochondria contact site integrity using the short ER-mitochondria SPLICS probe [38] in HeLa cells. Functionally, the probe employs a split-Green fluorescent protein (GFP) reporter system, which assembles into a fluorescent GFP entity only when the ER and outer mitochondrial membranes (OMM) are within <10 nm. This fluorescence arises from recomplementation of fluorescent GFP from the two GFP fragments that are separately localized to the ER and OMM (ER-$GFP_{\beta 11}$ and OMM-$GFP_{\beta 1-10}$). Cells were transfected with 3xFLAG-p2a-mCherry +/− 3xFLAG-CISD2 or 3xFLAG-BCL-2-p2a-mCherry +/− 3xFLAG-CISD2. Only mCherry-positive cells were analyzed. Fig. 7A shows representative acquisitions of SPLICS fluorescence, Hoechst staining and mCherry signal for each condition. Individual contact sites distinguishable as punctae were counted per cell (Fig. 7B). As an additional quantitative parameter, integrated density of SPLICS fluorescence were calculated per cell positive for mCherry (Fig. 7C). Overexpression of CISD2 alone did not have an effect on the number of ER-mitochondria contact sites when compared to the empty vector (EV) transfected conditions. However, BCL-2 overexpression reduced the number of contact sites per cell (number of punctae; Fig. 7B) as well as the total amount of contact sites per cell (integrated density being the total fluorescence of the SPLICS probe; Fig. 7C). ER-mitochondrial contact site integrity was further evaluated using an independent approach that is based on MAMtracker Green. In contrast to the SPLICS probe, MAMtracker Green does not rely on irreversible bimolecular fluorescence recomplementation (BiFC), but rather on the reversible dimerization-dependent GFP fluorescence [39]. Supplementary Fig. 4A displays representative acquisitions of MAMtracker Green fluorescence, Hoechst staining and mCherry signal for every condition. Mean MAMtracker Green fluorescence intensities were quantified per cell (Supplementary Fig. 4B). Here, similarly to the data obtained using the SPLICS probe, overexpression of BCL-2 alone reduced ER-mitochondrial contact compared to the EV-transfected condition, and co-overexpression of CISD2 with BCL-2 was able to rescue this. Correlating with our findings on ER-mitochondria Ca^{2+} flux, co-expression of CISD2 alleviated the inhibitory effect of BCL-2 overexpression on ER-mitochondria contact sites and restored the number and amount of contact sites per cell to the levels observed in EV-transfected cells. Hence, our findings indicate that i. BCL-2 disrupts ER-mitochondria contact sites and ii. CISD2 restores the BCL-2-evoked decrease in ER-mitochondria contact sites.

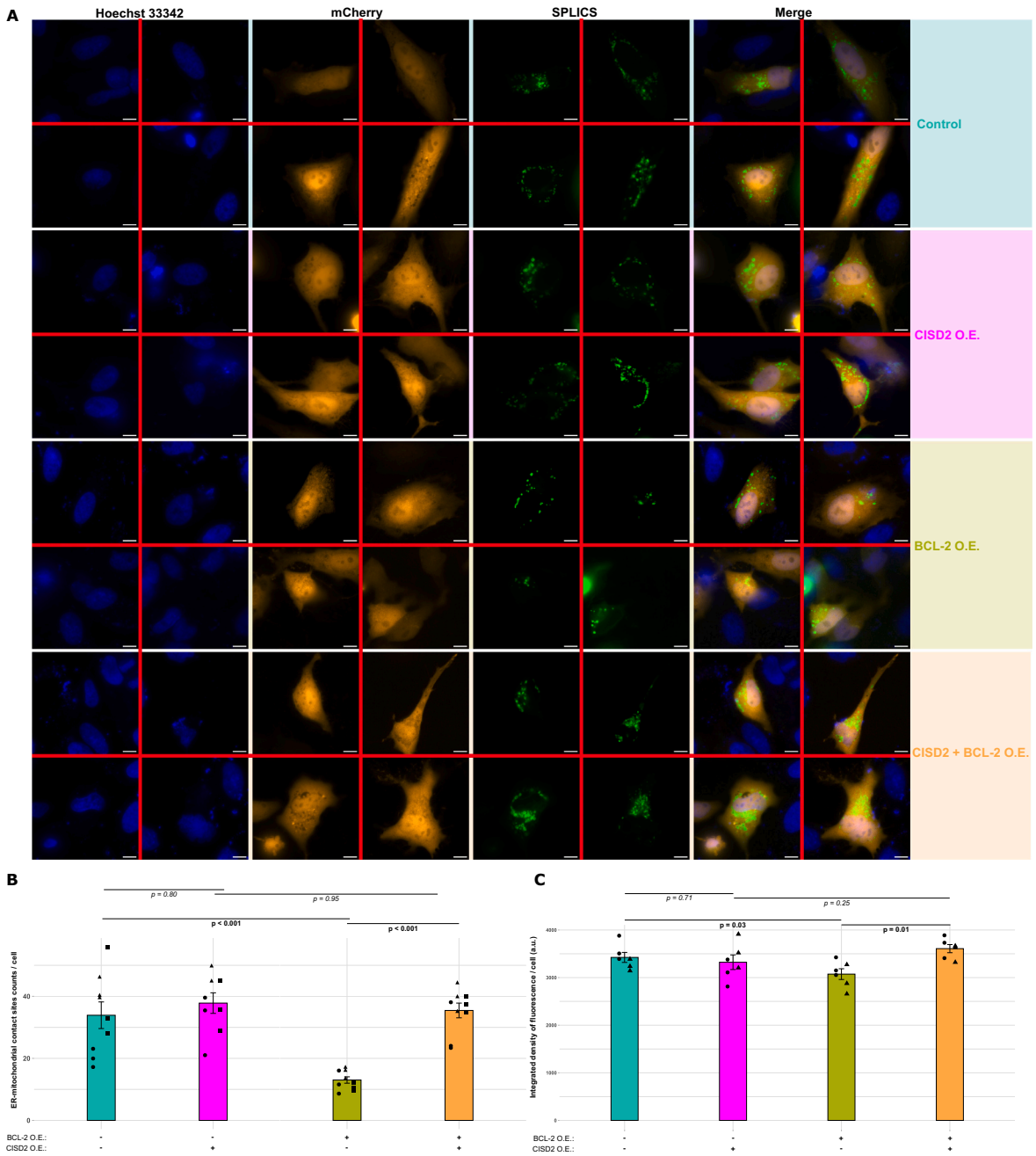

Fig. 7. A: Representative microscopic acquisitions, (four images per experimental condition), of Hoechst nuclear stain, mCherry and SPLICS fluorescence and merged images in HeLa cells. Scale bar corresponds to 10 μm. B: Quantification of at least 8 experiments per condition of averaged distinguishable ER-mitochondria contact foci per cell. Error bars correspond to standard error from mean. (Two-way ANOVA: interaction effect BCL-2 and CISD2 overexpression $F = 8.392$, $p = 0.007$). C: Quantification of 6 experiments per condition of averaged integrated density of fluorescence per cell. Error bars correspond to standard error from mean. (Two-way ANOVA: interaction effect BCL-2 and CISD2 overexpression $F = 7.4059$, $p = 0.01$).

3. Discussion

The main finding of this work is that CISD2 and BCL-2, both proteins that reside at the MAMs, interact with each other, thereby influencing their function at the ER-mitochondrial contact sites. The observed interaction between CISD2 and BCL-2 is in line with other work [13,26]. The binding of CISD2 to BCL-2 appears to have no impact on the canonical anti-apoptotic function of BCL-2. Furthermore, while CISD2 binds to the BH4 domain of BCL-2, the region responsible to interact with and inhibit IP_3Rs, CISD2 did not affect BCL-2 inhibition of IP_3R channel opening and IP_3R-mediated Ca^{2+} release in the cytosol. However, consistent with CISD2 being a MAM-resident protein, CISD2 alleviated BCL-2's inhibitory impact on ER-mitochondrial contact sites and Ca^{2+} transfers.

Here, using a variety of interaction assays, we found that CISD2 and BCL-2 are in vitro and *in cellulo* binding partners. Analysis of the purified cytosolic 2Fe-2S-cluster-containing CISD2 fragment and CISD2 proteins indicated a medium affinity interaction between both proteins with apparent K_D's in the sub-micromolar range. The combined evidence of direct interaction obtained through co-immunoprecipitation (Fig. 1B), MST (Fig. 1C) and BLI assays (Fig. 2A) provide high certainty of the interaction results given that the separate approaches compensate each other's limitations. Furthermore, the CISD2-binding region in BCL-2 appears in part to be executed through its BH4 domain with an

apparent K_D below 1 μM (Fig. 2B & C). Notably, the alteration of the BH4 domain in BCL-2^{K17D} resulted in a reduced binding affinity for CISD2 (Fig. 1C), confirming the important role of the BH4 domain in the interaction surface. These findings correlate and complement previous studies reporting BCL-2 binding to CISD2's C-terminal region [13,26]. Moreover, an integrated approach using a peptide array, deuterium exchange mass spectrometry and direct coupling analysis revealed that CISD2 targets 2 regions of BCL-2: amino acids 16–30, part of the BH4 domain, and amino acids 95–110, part of the BH3 domain. However, in that work, the affinity of the BCL-2/CISD2 complex or CISD2 binding to BCL-2's BH4 domain was not determined [26]. Moreover, in that study, the impact of BCL-2 on CISD2's 2Fe—2S cluster transfer activity was examined, showing an accelerating effect of BCL-2 on this CISD2 function. However, the impact of CISD2 on BCL-2's function was not determined.

BCL-2 executes multiple functions in cells. Via its hydrophobic cleft, BCL-2 operates as an anti-apoptotic and anti-autophagic protein by scaffolding the BH3 domain of pro-apoptotic proteins (such as BAX/BAK and activator BH3-only proteins) and essential autophagy proteins (such as BECLIN 1). Via its BH4 domain, BCL-2 functions as an inhibitor of intracellular Ca^{2+} release channels (such as IP_3Rs).

In previous work, it was found that CISD2 was necessary for ER-resident BCL-2 suppression of BECLIN 1-driven autophagy [13]. It was proposed that CISD2 served as a scaffold for the BCL-2-Beclin 1 complex, as in cells lacking CISD2, BECLIN 1 binding to BCL-2 was severely impaired. In our work, we focused on the anti-apoptotic function of BCL-2. In in vitro Bax-pore-formation assays and STS-evoked apoptosis experiments in HeLa cells, we did not find a major role for CISD2 in controlling BCL-2's anti-apoptotic function. In fact, BCL-2's anti-apoptotic function did not require CISD2, as BCL-2 overexpression was equally effective in protecting against STS-induced cell death in CISD2-KO cells compared to CISD2-proficient cells (Fig. 4). Moreover, CISD2 addition did not impact BCL-2 suppression of in vitro BAX-pore formation (Fig. 3). Of note, in the BAX-pore-formation assay, we used the cytosolic CISD2 fragment. While this CISD2 region is sufficient to interact with BCL-2, we cannot exclude that other elements outside this region are needed to exert a functional impact on BCL-2. Of note, in both assays, there seems a small – non-significant- stimulating effect of CISD2 on BCL-2 function. These findings may indicate a unique role for BCL-2 in autophagy versus apoptosis. However, in our work, we used wild-type BCL-2 while the previous work studying the impact on autophagy was performed using ER-targeted BCL-2 [13]. Furthermore, the effects may also be cell-type dependent, as our experiments were done in HeLa cells while the CISD2/BCL-2 interplay in autophagy was performed in HCT116 colon cancer cells [13]. Hence, further work will be needed, potentially using ER-directed BCL-2, a variety of cell types and stress inducers, to further elucidate the unique role for the CISD2/BCL-2 complex in autophagy versus apoptosis.

In addition to this, CISD2 has been reported to form a ternary complex with IP_3Rs and BCL-2 [13]. As CISD2 targets the BH4 domain of BCL-2, which is necessary and sufficient to inhibit IP_3Rs, we envisioned that CISD2, by competing with IP_3Rs for the BH4 domain of BCL-2, may potentially interfere with the inhibition of IP_3Rs by BCL-2. Moreover, in a cellular context it remained unknown whether CISD2 was required for IP_3R inhibition by BCL-2. However, consistent with purified BCL-2 binding to and inhibiting IP_3R channels, also in cells lacking CISD2, BCL-2 remained equally potent in inhibiting IP_3R-mediated Ca^{2+} release in the cytosol (Fig. 5 A, B, C, D & E). Moreover, overexpression of CISD2 or addition of purified CISD2 did not alleviate BCL-2 inhibition of IP_3R-mediated Ca^{2+} release and suppression of IP_3R single-channel opening, respectively (Fig. 5 F, G & Supplementary Fig. 3). In fact, we observed the opposite trend, showing that CISD2 overexpression appeared to be additive to BCL-2 in inhibiting IP_3R activity in single cells, as co-expression of BCL-2 and CISD2 increased the number of non-responding cells. It is possible that the rescue of mitochondrial Ca^{2+} buffering when CISD2 is co-overexpressed with BCL-2 contributed to this decrease in magnitude of cytosolic IP_3R-mediated Ca^{2+} release. In any case, these experiments suggest that CISD2 is not competing with IP_3Rs for binding to BCL-2's BH4 domain. However, we cannot rule out that CISD2 and BCL-2 interact with higher affinities in a cellular context and therefore, a certain degree of competition for IP_3Rs may still occur.

Consistent with previous studies [15,23,24,36], we found that both CISD2 and anti-apoptotic BCL-2 proteins reside at the MAMs (Fig. 6A). Moreover, in cells lacking CISD2, BCL-2 remained present in the MAMs, indicating that CISD2 is not critical for BCL-2's recruitment to ER-mitochondrial contact sites. However, more quantitative analyses will be needed to determine whether the presence of CISD2 could influence the amount of BCL-2 present in MAMs. In any case, we hypothesized that the CISD2/BCL-2-protein complex could operate at the ER-mitochondrial contact sites. We first assessed whether BCL-2 could impact ER-mitochondrial contact sites and ER-mitochondrial Ca^{2+} transfer. We observed a very prominent decrease in ER-mitochondrial Ca^{2+} transfer (Fig. 6C & D) and ER-mitochondrial contact sites (Fig. 7) upon BCL-2 overexpression, which CISD2 counteracted. A potential caveat of the use of probes for ER-mitochondrial contact site visualization based on the process of irreversible BiFC is the possibility to establish or force new contact sites. However, the foundational work reporting the SPLICS probes indicated that the expression of SPLICS per se did not result in an increased ER-mitochondrial Ca^{2+} transfer [40], indicating that SPLICS probes is not generating de novo ER-mitochondrial contact sites. However, the irreversible BiFC may affect dynamical impacts on ER-mitochondrial contact formation. Hence, we also used MAMtracker Green, which relies on the reversible process of dimerization-dependent GFP fluorescence [39]. Overall, the MAMtracker green provided very similar results. BCL-2 overexpression decreased ER-mitochondrial contact sites and/or increased spacing between ER and mitochondria, while co-overexpression of CISD2 was able to rescue the BCL-2-mediated decrease in ER-mitochondrial contact sites (Supplementary Fig. 4).

Given that CISD2 overexpression alone did not increase ER-mitochondrial contact or Ca^{2+} transfer, and a significant interaction effect existed between CISD2 and BCL-2 expression in rescuing ER-mitochondrial contact, we hypothesize that CISD2 can specifically counteract BCL-2 function in MAMs. However, a limitation in the current work is that direct evidence for the local CISD2/BCL-2-protein complex is actually responsible for the interplay between CISD2 and Bcl-2 on MAM formation and ER-mitochondrial Ca^{2+} transfer has not been presented. Hence, future work using a CISD2 mutant unable to bind to BCL-2 will be needed. Previous work by others indicated that the iron-sulfur cluster binding region in CISD2 interacts with BCL-2's BH4 domain [13,26]. Hence, a CISD2 protein carrying mutations in this region could yield a protein with reduced BCL-2 binding, thereby allowing to address this issue.

Irrespective of this limitation, to the best of our knowledge, this is the first report showing an impact of anti-apoptotic BCL-2 on ER-mitochondrial contact sites. Previous studies however already identified BCL-2-family members to reside at the MAMs and impact contact sites. For instance, BCL-2 related ovarian killer (BOK) was reported to tighten ER-mitochondrial contact [41], thereby rendering cells susceptible to pro-apoptotic Ca^{2+} transfer between ER and mitochondria. Another example is BCL-2like10 (NrH), which resides at the MAMs, where it forms a dynamic complex with IP_3R binding protein released with IP_3 (IRBIT). During apoptosis, BCL-2like10 together with dephosphorylated IRBIT is displaced from the MAMs. In the absence of IRBIT, BCL-2like10 reduced ER-mitochondrial contact sites. In combination with inhibition of IP_3Rs, this strongly attenuated ER-mitochondrial Ca^{2+} transfers, thereby impacting apoptosis susceptibility [42]. The BCL-2-mediated reduction of ER-mitochondrial contact sites as well as its modulation by CISD2 may provide a mechanistical explanation of the observed effects in ER-mitochondrial Ca^{2+} transfer. Taken together, these observations lead us to believe that CISD2 might be able to selectively finetune BCL-2's modulatory functioning over IP_3R

depending on their localization, be it within the MAMs or elsewhere. Hence, such CISD2/BCL-2 complexes within MAMs versus untethered ER sections may heavily diverge in terms of functional outputs, also due to the presence of a unique and distinct set of proteins [31]. However, further work will be needed to elucidate the cell physiological ramifications of BCL-2/CISD2 complexes at ER-mitochondrial contact sites and how these impact cell function including cellular metabolism and autophagy. In particular, the impact on mitochondrial physiology requires further study, especially considering the critical role of ER-mitochondrial contact and Ca^{2+} transfer in maintaining activity of several dehydrogenases involved in the Krebs cycle [10,31]. Furthermore, both BCL-2 and CISD2 have established roles in regulating autophagy, even in a Ca^{2+}-dependent fashion [13,43], while ER-mitochondrial interactions are also involved in both mitophagy and autophagy [31,44]. Thus, further research is needed to unravel the cell physiological impact of the BCL-2/CISD2 complex at the MAMs. Finally, of particular interest will be how WFS1, another WS related protein, can influence the BCL-2/CISD2 complex. A recent report showed that WFS1 and CISD2 interact, and overexpression of one can compensate for loss of function of the other [45]. Therefore, it will be of interest to assess whether overexpression of WFS1 can also counteract BCL-2 function in the MAMs.

4. Materials and methods

4.1. Chemicals and consumables

Unless specifically stated, all chemicals and consumables were obtained from Thermo Fischer (Merelbeke, Belgium).

4.2. Antibodies

Rabbit polyclonal anti-CISD2 (1:1000, ABClonal, A5231), mouse monoclonal anti-BCL-2 (1:500, Santa Cruz, sc-7382), rabbit anti-IP_3R1 (alias: Rbt03, 1:1000, homemade) [46], rabbit control IgG (Sino Biological Inc., CR1), mouse monoclonal anti-FLAG (Sigma, F3165), rabbit monoclonal anti-PARP (1:1000, Cell Signaling, 9532S).

4.3. Peptides

The following peptides, obtained from LifeTein (South Plainfield, NJ, USA) with purity $\geq$ 90 % were used and dissolved in dimethyl sulfoxide (DMSO) to prepare 10 mM stock solutions:

Biotin-BH4-BCL-2: Biotin-RTGYDNREIVMKYIHYKLSQRGYEW

Biotin-BH4-BCL-2scramble1: Biotin-WYEKQRSLHGIMYYVIEDRNTKGYR

Biotin-BH4-BCL-2scramble2: Biotin-KKINLRGDYSRQVMYEWTYGREIHY.

4.4. Plasmids and constructs

For the purification of human BCL-$2^{\Delta TM}$ WT/K17D, the cDNA sequences coding for C-terminally truncated BCL-2 was cloned in a pET45b(+) plasmid to allow purification using standard His-purification protocols, as previously described in [47]. The plasmid for the purification of human BCL-$2^{\Delta TM}$ K17D was obtained by PCR site-directed mutagenesis as previously described [48]. For the purification of $CISD2^{CYT}$ the cDNA sequence of the C-terminal domain, corresponding to the, cytosolic part of the human CISD2 protein was cloned in a pET21b(+) plasmid to allow purification using standard His-purification protocols [47]. For pulldowns with overexpressed 3XFLAG-BCL-2, pCMV24 constructs were created as described in [30]. pCMV24-(BCL-2)-p2a-mCherry constructs were created as described in [49]. All utilized constructs were sequenced and verified (LGC Genomics, Berlin, Germany). pCMV26 containing CISD2 was subcloned as follows: a gBlock™ containing the cDNA for CISD2 (Integrated DNA Technologies, Leuven, Belgium) with flanking 5' *Hin*dIII and 3' *Eco*RI restriction sites was restriction-ligated into an empty pCMV26 vector. Gblock sequence: 5'-ATATATGGATCCATGGTGCTGGAGAGCGTGGCCCGTATCGTGAAGGTGCAGCTCCCTGCATATCTGAAGCGGCTCCCAGTCCCTGAAAGCATTACCGGGTTCGCTAGGCTCACAGTTTCAGAATGGCTTCGGTTATTGCCTTTCCTTGGTGTACTCGCACTTCTTGGCTACCTTGCAGTTCGTCCATTCCTCCCGAAGAAGAAACAACAGAAGGATAGCTTGATTAATCTTAAAATACAAAAGGAAAATCCGAAAGTAGTGAATGAAATAAACATTGAAGATTTGTGTCTTACTAAAGCAGCTTATTGTAGGTGTTGGCGTTCTAAAACGTTTCCTGCCTGCGATGGTTCACATAATAAACACAATGAATTGACAGGAGATAATGTGGGTCCACTAATACTGAAGTACCCATACGATGTTCCAGATTACGCTAAGAAAGAAGTATAGGAATTCGCGCGC-3′. pCMV-CEPIA2mt [37] was a gift from Masamitsu Iino (Addgene plasmid # 58218; http://n2t.net/addgene:58218; RRID:Addgene_58218).

4.5. Cell culture and transfections

HeLa cells were cultured at 37 °C, 5 % CO_2 in Dulbecco's Modified Eagle's Medium (DMEM), supplemented with 5 % fetal calf serum, 100 IU/mL penicillin and 100 μg/mL streptomycin, 2 mM Glutamax. HeLa cells were seeded 24 h (h) before transfection and were transfected using Mirus TransIT-X2 transfection reagent (Mirus Bio, WI, USA) with a 2:1 transfection reagent in μL per μg DNA.

4.6. Generation of CISD2 KO and Cas9 control HeLa cells

HeLa cells were seeded in 6 well plates and grown until aproximately 80 % confluence and transfected with 5 μg of pSpCas9(BB)-2A-Puro vector vector containing a guideRNA for CISD2 in the case of CISD2 KO cells or an empty control vector in the case of Cas9 control cells. pSpCas9(BB)-2A-Puro (PX459) was a gift from Feng Zhang (Addgene plasmid # 48139; http://n2t.net/addgene:48139; RRID:Addgene_48139) [50]. Transfected cells were selected by culturing the cells for 48 h in presence of 3 μg/mL puromycin. Knockout of CISD2 was verified via immunoblotting. Guide RNA sequence (GGAGCTGCACCTTCACGATA) was obtained from Synthego (Redwood City, CA, USA).

4.7. Protein purification

Purified proteins were generated in BL21 *Escherichia coli*. After growth, the bacteria were diluted to an A600 of approximately 0.2, followed by a heat shock at 40 °C for 2 h. Isopropyl-d-1-thiogalactopyranoside was added (100 μM) to induce protein expression at 20 °C for 2 h 30 min. Bacteria were harvested by centrifugation at 5000 *g* for 10 min and around 10 g of bacterial pellet was resuspended in 60 mL lysis buffer (150 mM NaCl, 10 mM Tris, 30 mM imidazole, 20 % glycerol, pH 7.4). Samples were sonicated three times at 20 kHz (5 × 10 s) with incubation at 4 °C in between each sonication round. Subsequently the mixture was centrifuged at 35,000 rpm for 40 min. Supernatant was collected and incubated with nickel-nitrilotriacetic acid resin (Ni–NTA Sepharose™ 6 Fast Flow) for 20 h at 4 °C. All proteins (CISD2_6xHis, 6xHis_BCL-$2^{\Delta TM,\ WT}$ and 6xHis_BCL-$2^{\Delta TM,\ K17D}$) were eluted using lysis buffer containing 500 mM imidazole. Finally, for each purification around 3 mL of purified protein was dialyzed using a Slide-A-Lyzer®Dialysis Cassette G2 (ThermoFisher Scientific) with a cutoff of 10 kDa, three times in 500 mL phosphate buffered saline without Ca^{2+}/Mg^{2+} (PBS −/−, Gibco) for 1 h. Any formed protein aggregates were removed by centrifugation (600 s on 16.1 g at 4 °C) and filtration through a syringe filter (Millex, Hydrophilic PTFE membrane, 0.22 μM pore size). Concentration of the purified proteins was determined using both nanodrop (A280) and Bradford Reagent (ThermoFisher Scientific). The purity and quality of each purification was evaluated by Coomassie blue staining of the gels using Imperial Protein Stain reagent (ThermoFisher Scientific). Additionally, the identity of purified proteins was verified through immunoblotting, performed as previously described

[51].

4.8. Co-immunoprecipitation assays

To pull down CISD2^{CYT} in a mixture of 30 μg CISD2^{CYT} and 10 μg BCL-2$^{\Delta TM}$, 5 μg of either the CISD2 antibody or an aspecific rabbit IgG control (Sino Biological, Bejing, China) were incubated with 20 uL of Dynabeads and washed with PBS 0.2 % Tween. Protein-beads mixtures were incubated overnight at 4 °C in phosphate-buffered saline (PBS). The next day, beads were washed five times with PBS, after which bound samples were eluted using PBS containing 0.2 % SDS (SDS elution buffer).

For the co-immunoprecipitation experiments using cell lysates, HeLa WT cells and HeLa CISD2 KO cells were seeded 24 h before transfection. Cells were transfected with 400 ng pCMV24-3xFLAG-empty vector or pCMV24-3xFLAG-BCL-2 and harvested by scraping in ice cold PBS. Cells were lysed with a 3-((3-cholamidopropyl) dimethylammonio)-1-propanesulfonate (CHAPS) based buffer (50 mM Tris, 100 mM NaCl, 2 mM Ethylenediaminetetraacetic acid, 50 mM NaF, 1 mM Na_3VO_4, 1 % CHAPS and protease inhibitor tablets (Roche, Basel, Switzerland) according to manufacturer's instructions). 2.5 μg of anti-FLAG antibody was incubated with 10 μL of Dynabeads and washed with PBS 0.2 % Tween. Beads were incubated with 400 μg protein lysate overnight at 4 °C in CHAPS lysis buffer. The next day, samples were washed with PBS, and eluted using SDS elution buffer (0.2 % SDS + 0.01 % Tween pH 8).

4.9. Immunoblotting

NuPAGE™ LDS Sample Buffer was added to all immunoblot samples which following boiling were ran on NuPAGE™ 4–12 % Bis-Tris gels. Subsequently, proteins were transferred on a polyvinylidene fluoride membrane. Membranes were blocked with Tris-buffered saline (TBS) containing 5 % milk powder and 0.1 % Tween and incubated with primary antibody overnight. The next day, membranes were incubated for 1 h with secondary horseradish peroxidase-linked antibodies in TBS 0.1 % Tween. Pierce™ ECL chemiluminescent western blot reagent was used for detection in a Chemidoc imaging system (Bio-Rad, CA, USA).

4.10. Microscale thermophoresis

Purified CISD2^{CYT} protein was fluorescently labeled using the Monolith His-Tag Labeling Kit RED-tris-NTA 2nd Generation (Nano Temper Technologies, Munich, Germany) and binding affinities for either BCL-2$^{\Delta TM}$ and BCL-2$^{\Delta TM,\ K17D}$ were evaluated using MicroScale Thermophoresis using a Monolith NT automated instrument (Nano Temper Technologies), in a similar way as previously published [52]. The concentration of labeled CISD2^{CYT} was kept constant at 10 nM, whereas BCL-2$^{\Delta TM}$ and BCL-2$^{\Delta TM,\ K17D}$ proteins were titrated down from 10 μM in a two-fold dilution series of twelve. Measurements were performed with a pico-red laser channel at 15 % excitation power and 40 % MST power in steady-state conditions using premium capillaries and subsequently recorded on a Monolith instrument. All experiments were repeated three times for each condition using freshly thawed proteins with two technical replicates for each biological replicate.

4.11. Biolayer interferometry

4.11.1. AR2G biosensor

Purified BCL-2$^{\Delta TM,\ WT}$ was immobilized on Octet® Amine Reactive Second generation (AR2G) Biosensors in the Octet® Red system in a similar way as previously published [52] and used to evaluate its binding affinity and binding kinetics for purified CISD2^{CYT}. Before the start of the experiment, the sensors were hydrated in ultrapure MilliQ water. Upon measurement, the sensors were equilibrated for 60 s in MilliQ water after which we activated the AR2G biosensors via a 500 s reaction in a mixture of 20 mM EDC (1-ethyl-3[3-dimethylaminopropyl] carbodiimide hydrochloride) and 10 mM sulfo-NHS (N-hydroxysulfosuccinimide) to generate highly reactive NHS esters. Subsequently, the selected ligand was immobilized/loaded to the sensors through formation of highly stable amide bonds in a 10 mM acetate buffer (pH 5) over 600 s. The remaining reactive NHS esters on the biosensor were quenched in a 1 M ethanolamine solution for 300 s. Once the ligand was correctly loaded, we measured a baseline in the binding buffer (DPBS, no Ca^{2+}, no Mg^{2+} (Gibco™); 0.02 % tween) after which different concentrations of analyte were used to assess the K_{on} rate of our ligand towards our analyte in the association phase (1000 s). To assess the K_{off} rates of the ligand towards the analyte, the sensors were again submerged in binding buffer to allow dissociation of the analyte (2000 s). As a reference we used a ligand-loaded sensor which was incubated in binding buffer during both the association and the dissociation phase. We also performed a naked sensor control utilizing the highest [CISD2^{CYT}] in our analysis after performing the activation and quenching as performed in all other conditions (data not shown).

4.11.2. SA biosensor

Commercially obtained biotinylated peptides (loaded ligands: biotin-BH4$^{BCL\text{-}2}$, biotin-BH4^{scr}, and biotin-BH4^{scr2}) were immobilized on Octet® streptavidine (SA) Biosensors in the Octet® Red system and used to evaluate its binding affinity and binding kinetics for purified CISD2-^{CYT}. Before the start of the experiment, the sensors were hydrated in ultrapure MilliQ water. Upon measurement, the sensors were equilibrated for 60 s in MilliQ water after which the selected ligand was immobilized/loaded to the sensors for 100 s or 60 s (for biotin-BH4$^{BCL\text{-}2}$ or biotin-BH4$^{scr(2)}$ respectively). Once the ligand was correctly loaded, we measured a baseline in the binding buffer after which different concentrations of analyte (CISD2^{CYT} and bovine serum albumin) were used to assess the K_{on} rate of our ligand towards our analyte in the association phase (2000 s). To assess the K_{off} rates of the ligand towards the analytes, the sensors were again submerged in binding buffer to allow dissociation of the analyte (4000 s). As a reference we used a ligand-loaded sensor which was incubated in binding buffer during both the association and the dissociation phase. We also performed a naked sensor control utilizing the highest [CISD2^{CYT}] in our analysis after performing the activation and quenching as performed in all other conditions (data not shown).

4.12. SMAC-mCherry release assay

BMK Bax/Bak DKO cells expressing SMAC-mCherry were plated in a 384 Perkin-Elmer Pheno plate at 6000 cells per well. 24 h after seeding, purified proteins were thawed on ice and centrifuged at max speed (15 000 *g*) to remove protein aggregates. 8 point titration curves of purified BCL-2$^{\Delta TM}$ were created in a 384-well source plate containing trehalose-hepes buffer (THB) (300 mM Trehalose, 10 mM HEPES-KOH pH 7.7, 80 mM KCl, 1 mM EGTA, 1 mM EDTA, 0.1 % BSA and 5 mM succinate) with 5 μM DRAQ5™ Fluorescent Probe Solution, 0.0025 % *w/v* digitonin with 20 nM purified Bax (in the case of negative control), or 20 nM purified Bax and 0.5 nM cBID (in the case of the positive control and BCL-2 dilution series), and 2 μM of purified CISD2^{cyt} or an equal volume of PBS. Using the Vantage automated liquid handler, media was removed from the cells and cells were washed twice using 30 μL of THB. 25 μL of volume from the source plate was added to the cells. Cells were incubated for 60–80 min at 37 °C, 5 % CO_2 and imaged on an Opera Phenix microscope. Nuclei and mitochondria were imaged and processed using PerkinElmer Harmony software, where cells were segmented using the DRAQ5 channel and the mean intensity of SMAC-mCherry for each cell was calculated.

4.13. Staurosporine-induced apoptosis experiments

HeLa cells were seeded 24 h before transfection. HeLa WT or CISD2 KO cells were transfected with 400 ng pCMV24-3xFLAG-BCL-2 or empty

vector. In the case of CISD2 and BCL-2 co-overexpression, HeLa cells were transfected with 400 ng pCMV24-3xFLAG-BCL-2 or empty vector and 500 ng pCMV26-CISD2 or EV. 48 h after transfection, cells were treated with 500 nM of staurosporine or with DMSO for 6 h. After treatment, cells were harvested by scraping on ice, and lysed with CHAPS buffer. Samples were analyzed via immunoblotting.

4.14. Single cell ratiometric Ca^{2+} imaging

For FURA-2 measurements, a Nikon TI2-E inverted microscope equipped with a 20 × 0.5 NA Plan Fluor DIC N2 air objective and a pco. edge 4.2bi sCMOS camera was used. FURA-2 was alternatingly excited at a 2 s interval using a CoolLED pE-300 ultra/pE-340 lamp set at 340 nm and 380 nm (CoolLED, Andover, UK), and using a dichroic mirror FF02-409/LP-25 (Semrock, New York, USA) and a bandpass emission filter 515/30 (Semrock, Rochester, USA). mCherry was visualized using a CoolLed pR-4000 lamp (CoolLED, Andover, UK) at 550 nm, and using the cubical excitation filterset FF01–378/474/554/635 and a bandpass emission filter 595/31 (Semrock, Rochester, USA). All cells were seeded in 4 chamber slides with coverslips (IBL, Gerasdorf bei Wien, Austria). WT and CISD2 KO HeLa cells were transfected with 200 ng BCL-2-p2a-mCherry or p2a-mCherry. In the co-overexpression experiments, HeLa cells were transfected with 150 ng BCL-2-p2a-mCherry or p2a-mCherry and 450 ng CISD2 or EV. Two days after transfection, cells were loaded for 30 min, at room temperature, with 1 μM FURA-2-AM (AnaSpec, Fremont, CA, USA) in modified Krebs buffer (135 mM NaCl, 6.2 mM KCl, 1.2 mM $MgCl_2$, 12 mM HEPES, pH 7.3, 11.5 mM glucose and 1.5 mM $CaCl_2$). Cells were washed once with modified Krebs and the FURA-2-AM was allowed to de-esterify during 30 min at room temperature. After measuring for about 30 s, 3 mM ethylene glycol-bis(β-aminoethyl ether)-N,N,N′,N′-tetraacetic acid (EGTA) in Krebs without Ca^{2+} was added to chelate extracellular Ca^{2+}. Responses of mCherry positive cells to 2 μM ATP were measured. As a control, 2.5 μM of ionomycin was added at the end of the acquisition. Data was quantified using a custom ImageJ script, which can be found on: https://github.com/jensloncke/ImageJ_macros/tree/master/FURA%20transfected%20cells. Relevant response parameters, such as area under curve, were extracted using a custom Python script: https://github.com/jensloncke/LMCS-python-scripts/tree/main/Quantify%20agonist%20response. Cells that detached, or did not respond to either 2 μM ATP or 2.5 μM ionomycin were excluded from analysis.

4.15. Single-channel electrophysiology recordings

Nuclei isolated from DT40 IP_3R 3KO cells stably transfected with rat IP_3R1 were prepared using homogenization methods as outlined previously [53]. Subsequently, a 3 μL portion of the nuclear suspension was placed in a 3 mL bath solution comprising 140 mM KCl, 10 mM Hepes, 500 μM BAPTA, and 246 nM free Ca^{2+} at pH 7.1. Before patching, the nuclei adhered to a plastic culture dish for 10 min. Subsequently, single-channel potassium currents of IP_3R1 were measured in the on-nucleus patch-clamp configuration utilizing pCLAMP 9 and an Axopatch 200B amplifier (Molecular Devices, Sunnydale, CA, USA). The pipette solution consisted of 140 mM KCl, 10 mM Hepes, 1 μM IP_3, 200 nM free Ca^{2+}, 5 mM ATP, and either $CISD2^{CYT}$, $BCL\text{-}2^{\Delta TM}$, or control solution as indicated. Traces were recorded as consecutive 3-s sweeps at −100 mV, sampled at 20 kHz, and filtered at 5 kHz. A minimum of 15 s of recordings were taken into consideration for data analysis. The pipette resistances typically ranged around 20 MΩ, and seal resistances were consistently >5 GΩ. Single-channel openings were identified using half-threshold crossing criteria through the event detection protocol in Clampfit 9. The assumption was made that the maximum number of discrete stacked events observed during the experiment represented the number of channels in a given nuclear patch. Only patches with a single apparent channel were included in the analyses. Po was calculated using Clampfit 9 and Origin 6 software (Origin Lab, Northampton, MA, USA).

4.16. Purification of HeLa MAM fractions through subcellular fractionation

Subcellular fractions were purified from Cas9 control and CISD2-KO HeLa cells as previously described [54]. In brief, HeLa cells were homogenized and after several centrifugation steps, a crude mitochondrial fraction is obtained separately from the ER and cytosolic fractions. After ultracentrifugation of the crude mitochondrial fraction in a Percoll® (Santa Cruz Biotechnology Inc., Dallas, USA) gradient, MAM and pure mitochondrial fractions were obtained.

4.17. Single cell mitochondrial Ca^{2+} imaging

A Nikon TI2-E inverted microscope equipped with a 40 × 1.3 NA Plan Fluor DIC H N2 Oil objective and a pco.edge 4.2bi sCMOS camera was used. Green mtCEPIA was excited at an interval of 2 s. Green mtCEPIA and mCherry were both excited at 470 nm and 550 nm respectively, using a CoolLed pR-4000 lamp, and using the cubical excitation filterset FF01–378/474/554/635 and bandpass emission filters of 515/30 and 595/31, respectively. All cells were seeded in 4 chamber slides with coverslips. HeLa cells were transfected with 80 ng G-mtCEPIA2, 80 ng BCL-2-p2a-mCherry or p2a-mCherry and 240 ng CISD2 or EV. Two days after transfection, cells were imaged in modified Krebs buffer. After measuring for 30 s, 3 mM EGTA in Krebs without Ca^{2+} was added to chelate extracellular Ca^{2+}. Responses of mCherry positive cells to 2 μM ATP were measured. As a control, 2.5 μM of ionomycin was added at the end of the acquisition. Data was quantified using a custom ImageJ script, which can be found on: https://github.com/jensloncke/ImageJ_macros/tree/master/Fluo-4%20transfected%20cells. Relevant response parameters, such as area under curve, were extracted using a custom Python script: https://github.com/jensloncke/LMCS-python-scripts/tree/main/Quantify%20agonist%20response. Cells that detached, or did not respond to either 2 μM ATP or 2.5 μM ionomycin were excluded from analysis.

4.18. Imaging of ER-mitochondrial contact sites using Mt-ER short SPLICS probe and MAMtracker Green

ER-mitochondrial contact sites were specifically detected using the SPLICS Mt-ER Short P2A probe. SPLICS Mt-ER Short P2A was a gift from Marisa Brini & Tito Calì (Addgene plasmid # 164108; http://n2t.net/addgene:164108; RRID:Addgene_164108) [38]. Additionally, we used the MAMtracker Green probe [39]. The p-MAMtracker Green vector was a kind gift from Koji Yamanaka (Nagoya University, Japan). A Nikon TI2-E inverted microscope equipped with a 40 × 1.3 NA Plan Fluor DIC H N2 Oil objective with intermediate 1.5× magnification and a pco.edge 4.2bi sCMOS camera was used. SPLICS and MAMtracker Green were both excited at 470 nm, using a CoolLed pR-4000 lamp and using the cubical excitation filterset FF01–378/474/554/635 and bandpass emission filters of 515/30. mCherry was excited at 550 nm, using a CoolLed pR-4000 lamp, and using the cubical excitation filterset FF01–378/474/554/635 and a bandpass emission filter 595/31. Hoechst was excited at 350 nm using a CoolLed pR-4000 lamp, and using the cubical excitation filterset FF01-378/474/554/635. All cells were seeded in 4 chamber slides with coverslips. HeLa cells were transfected with 300 ng SPLICS or 150 ng MAMtracker Green, 80 ng BCL-2-p2a-mCherry or p2a-mCherry and 240 ng CISD2 or EV. Two days after transfection, cells were stained with Hoechst and imaged in modified Krebs buffer. 2D images were simultaneously acquired of Hoechst stains, SPLICS or MAMtracker Green signal, mCherry signal and brightfield images. Individual ER-mitochondrial contact sites were counted using the Cell Counter plugin in ImageJ. When multiple contact sites close together were non-resolvable due to the limitations of the acquisition set-up, only a single contact site was counted. Integrated densities of fluorescence and mean fluorescence intensities were calculated using ImageJ.

4.19. Data analysis

Quantification of immunoblots was performed using the FIJI software [55]. MST data processing was performed monolith analysis software (MO.Affinity Analysis v2.3). The Prism software (GraphPad Prism 8.4.2) was used to plot the processed data, fit a nonlinear regression curve (Sigmoidal, 4PL, X is concentration) and calculate the dissociation constant (K_D) for each condition. BLI data was obtained from the measurement software ForteBio Data Acquisition 9.0.0.48 was processed using the Octet red 96 analysis software (ForteBio Data Analysis 9.0). Data processing was performed through the following standardized steps: 1) Subtraction of the naked loaded sensor measurement. 2) Y-axis alignment (baseline). 3) Inter-step correction alignment (dissociation). 4) Savitzky-Golay filtering. 5) Partial local fitting using a one-by-one interaction model. The obtained steady-state results were plotted and analyzed using GraphPad Prism 8.4.2. and fitted using a nonlinear regression curve (Sigmoidal, 4PL, X is concentration). All other plots were created using the ggplot2 package [56] in the R programming language [57]. To statistically compare differences in co-immunoprecipitated IP_3R with immunoprecipitated BCL-2, a Welch's *t*-test was performed, after checking normality of residuals via Shapiro-Wilk normality testing and assessing equality of variances with the Levene test. IC_{50} curves in the SMAC-mCherry release assay were fitted using a four-parameter model using the drc Bioconductor package [58]. For comparing differences in IC_{50} values in the SMAC-mCherry release assay, a non-parametric Wilcoxon rank sum exact test was used due to non-normal distribution of the data. For hypothesis testing, assumptions of normal distribution of residuals and equality of variances was checked via Shapiro-Wilk testing and Levene testing, respectively. In the event of both of the assumptions being fulfilled, a two-way ANOVA was performed, followed by Tukey-corrected pairwise *t*-tests. In case of unequal variances within conditions, ANOVA was corrected for heteroskedasticity. When assumption of normal distribution was not fulfilled, a non-parametric Kruskal-Wallis was performed, followed by pairwise Mann-Whitney *U* tests. For the post-hoc comparisons in Fig. 4, one-tailed pairwise paired Mann-Whitney U tests were carried out. In the case of integrated fluorescence densities in the SPLICS assay, paired post-hoc t-tests were carried out. Two-way ANOVA was carried out using the car package [59] and Tukey-corrected post-hoc tests were performed by using the stats package. Kruskal Wallis tests and Mann-Whitney U tests were performed using the stats package. Microscopy data was acquired using the NIS elements software and numerically extracted in FIJI using custom macros. Data was further processed in Python using the numpy [60], pandas [61] and plotly packages. Fitting of data from SMAC-mCherry release assay was done using the drc bioconductor package. Welch's t-test was performed using base R.

Authorship statement

All authors should have made substantial contributions to all of the following: (1) the conception and design of the study, or acquisition of data, or analysis and interpretation of data, (2) drafting the article or revising it critically for important intellectual content, (3) final approval of the version to be submitted.

Funding

Research supported by Research Foundation—Flanders (FWO) to G. B. (G081821N, G094522N), the KU Leuven Research Council (C14/19/099 and AKUL/19/34) and the Central European Leuven Strategic Alliance (CELSA/23/031 and CELSA/23/032). G.B., J.B.P. and D.I.Y. are partners of the FWO Scientific Research Network CaSign (W0.014.22N). I.D.R. is supported by a PhD fellowship from the FWO (1131322N|1131324N). T.V is supported by a Post-doctoral fellowship from the FWO (12ZG121N).

CRediT authorship contribution statement

Jens Loncke: Writing – original draft, Methodology, Investigation, Formal analysis, Data curation, Conceptualization. **Ian de Ridder:** Writing – original draft, Methodology, Investigation, Formal analysis, Data curation. **Justin Kale:** Writing – review & editing, Visualization, Methodology, Formal analysis, Data curation. **Larry Wagner:** Writing – review & editing, Visualization, Methodology, Investigation, Formal analysis, Data curation. **Allen Kaasik:** Writing – review & editing, Resources, Funding acquisition, Conceptualization. **Jan B. Parys:** Writing – review & editing, Supervision, Conceptualization. **Martijn Kerkhofs:** Writing – review & editing, Supervision. **David W. Andrews:** Writing – review & editing, Supervision, Methodology, Conceptualization. **David Yule:** Writing – review & editing, Supervision, Methodology, Conceptualization. **Tim Vervliet:** Writing – review & editing, Supervision, Project administration, Funding acquisition, Conceptualization. **Geert Bultynck:** Writing – review & editing, Supervision, Project administration, Funding acquisition, Conceptualization.

Declaration of competing interest

The authors have no conflicts of interest to report.

Data availability

The underlying data will be available via KU Leuven RDR: https://doi.org/10.48804/VUBLPB.

Acknowledgements

The authors thank Anja Florizoone, Rita La Rovere and Tomas Luyten for excellent technical help. We are grateful to Dr. Cali (University of Padova, Italy) to provide SPLICS probes and to Dr. Yamanaka (Nagoya University, Japan), for providing the MAMtracker Green probe.

Appendix A. Supplementary data

Supplementary data to this article can be found online at https://doi.org/10.1016/j.bbamcr.2024.119857.

References

[1] J. Kale, E.J. Osterlund, D.W. Andrews, BCL-2 family proteins: changing partners in the dance towards death, Cell Death & Differentiation 25 (2018) 65–80.
[2] R. Singh, A. Letai, K. Sarosiek, Regulation of apoptosis in health and disease: the balancing act of BCL-2 family proteins, Nat. Rev. Mol. Cell Biol. 20 (2019) 175–193.
[3] H. Kalkavan, D.R. Green, MOMP, cell suicide as a BCL-2 family business, Cell Death & Differentiation 25 (2018) 46–55.
[4] L. Galluzzi, I. Vitale, S.A. Aaronson, J.M. Abrams, D. Adam, P. Agostinis, E. S. Alnemri, L. Altucci, I. Amelio, D.W. Andrews, M. Annicchiarico-Petruzzelli, A. V. Antonov, E. Arama, E.H. Baehrecke, N.A. Barlev, N.G. Bazan, F. Bernassola, M.J. M. Bertrand, K. Bianchi, M.V. Blagosklonny, K. Blomgren, C. Borner, P. Boya, C. Brenner, M. Campanella, E. Candi, D. Carmona-Gutierrez, F. Cecconi, F.K. M. Chan, N.S. Chandel, E.H. Cheng, J.E. Chipuk, J.A. Cidlowski, A. Ciechanover, G. M. Cohen, M. Conrad, J.R. Cubillos-Ruiz, P.E. Czabotar, V. D'Angiolella, T. M. Dawson, V.L. Dawson, V. De Laurenzi, R. De Maria, K.-M. Debatin, R. J. DeBerardinis, M. Deshmukh, N. Di Daniele, F. Di Virgilio, V.M. Dixit, S.J. Dixon, C.S. Duckett, B.D. Dynlacht, W.S. El-Deiry, J.W. Elrod, G.M. Fimia, S. Fulda, A. J. García-Sáez, A.D. Garg, C. Garrido, E. Gavathiotis, P. Golstein, E. Gottlieb, D. R. Green, L.A. Greene, H. Gronemeyer, A. Gross, G. Hajnoczky, J.M. Hardwick, I. S. Harris, M.O. Hengartner, C. Hetz, H. Ichijo, M. Jäättelä, B. Joseph, P.J. Jost, P. P. Juin, W.J. Kaiser, M. Karin, T. Kaufmann, O. Kepp, A. Kimchi, R.N. Kitsis, D. J. Klionsky, R.A. Knight, S. Kumar, S.W. Lee, J.J. Lemasters, B. Levine, A. Linkermann, S.A. Lipton, R.A. Lockshin, C. López-Otín, S.W. Lowe, T. Luedde, E. Lugli, M. MacFarlane, F. Madeo, M. Malewicz, W. Malorni, G. Manic, J.-C. Marine, S.J. Martin, J.-C. Martinou, J.P. Medema, P. Mehlen, P. Meier, S. Melino, E.A. Miao, J.D. Molkentin, U.M. Moll, C. Muñoz-Pinedo, S. Nagata, G. Nuñez, A. Oberst, M. Oren, M. Overholtzer, M. Pagano, T. Panaretakis, M. Pasparakis, J.M. Penninger, D.M. Pereira, S. Pervaiz, M.E. Peter, M. Piacentini, P. Pinton, J.H.M. Prehn, H. Puthalakath, G.A. Rabinovich, M. Rehm, R. Rizzuto, C. M.P. Rodrigues, D.C. Rubinsztein, T. Rudel, K.M. Ryan, E. Sayan, L. Scorrano, F. Shao, Y. Shi, J. Silke, H.-U. Simon, A. Sistigu, B.R. Stockwell, A. Strasser,

G. Szabadkai, S.W.G. Tait, D. Tang, N. Tavernarakis, A. Thorburn, Y. Tsujimoto, B. Turk, T. Vanden Berghe, P. Vandenabeele, M.G. Vander Heiden, A. Villunger, H. W. Virgin, K.H. Vousden, D. Vucic, E.F. Wagner, H. Walczak, D. Wallach, Y. Wang, J.A. Wells, W. Wood, J. Yuan, Z. Zakeri, B. Zhivotovsky, L. Zitvogel, G. Melino, G. Kroemer, Molecular mechanisms of cell death: recommendations of the Nomenclature Committee on Cell Death, Cell Death & Differentiation 25 (2018) (2018) 486–541.

[5] T. Vervliet, J.B. Parys, G. Bultynck, Bcl-2 proteins and calcium signaling: complexity beneath the surface, Oncogene 35 (2016) 5079–5092.

[6] A. Danese, S. Leo, A. Rimessi, M.R. Wieckowski, F. Fiorica, C. Giorgi, P. Pinton, Cell death as a result of calcium signaling modulation: a cancer-centric prospective, Biochimica et Biophysica Acta (BBA) - Molecular Cell Research 1868 (2021) 119061.

[7] J.K. Foskett, C. White, K.-H. Cheung, D.-O.D. Mak, Inositol trisphosphate receptor Ca^{2+} release channels, Physiol. Rev. 87 (2007) 593–658.

[8] G. Szabadkai, K. Bianchi, P. Várnai, D. De Stefani, M.R. Wieckowski, D. Cavagna, A. I. Nagy, T. Balla, R. Rizzuto, Chaperone-mediated coupling of endoplasmic reticulum and mitochondrial Ca^{2+} channels, J. Cell Biol. 175 (2006) 901–911.

[9] G. Csordás, A.P. Thomas, G. Hajnóczky, Quasi-synaptic calcium signal transmission between endoplasmic reticulum and mitochondria, EMBO J. 18 (1999) 96–108.

[10] J. Loncke, A. Kaasik, I. Bezprozvanny, J.B. Parys, M. Kerkhofs, G. Bultynck, Balancing ER-mitochondrial Ca^{2+} fluxes in health and disease, Trends Cell Biol. 31 (2021) 598–612.

[11] Y.-P. Rong, G. Bultynck, A.S. Aromolaran, F. Zhong, J.B. Parys, H. De Smedt, G. A. Mignery, H.L. Roderick, M.D. Bootman, C.W. Distelhorst, The BH4 domain of Bcl-2 inhibits ER calcium release and apoptosis by binding the regulatory and coupling domain of the IP_3 receptor, Proc. Natl. Acad. Sci. 106 (2009) 14397–14402.

[12] P. Pinton, D. Ferrari, P. Magalhães, K. Schulze-Osthoff, F. Di Virgilio, T. Pozzan, R. Rizzuto, Reduced loading of intracellular ca(2+) stores and downregulation of capacitative Ca^{2+} influx in Bcl-2-overexpressing cells, J. Cell Biol. 148 (2000) 857–862.

[13] N.C. Chang, M. Nguyen, M. Germain, G.C. Shore, Antagonism of Beclin 1-dependent autophagy by BCL-2 at the endoplasmic reticulum requires NAF-1, EMBO J. 29 (2010) 606–618.

[14] O. Karmi, Y.-S. Sohn, S.I. Zandalinas, L. Rowland, S.D. King, R. Nechushtai, R. Mittler, Disrupting CISD2 function in cancer cells primarily impacts mitochondrial labile iron levels and triggers TXNIP expression, Free Radic. Biol. Med. 176 (2021) 92–104.

[15] J. Loncke, T. Vervliet, J.B. Parys, A. Kaasik, G. Bultynck, Uniting the divergent Wolfram syndrome-linked genes, WFS1 and CISD2, as modulators of Ca^{2+} signaling, Science Signaling 14 (2021) eabc6165.

[16] Z.-Q. Shen, Y.-L. Huang, Y.-C. Teng, T.-W. Wang, C.-H. Kao, C.-H. Yeh, T.-F. Tsai, CISD2 maintains cellular homeostasis, Biochimica et Biophysica Acta (BBA) - Molecular Cell Research 1868 (2021) 118954.

[17] Y.-S. Sohn, S. Tamir, L. Song, D. Michaeli, I. Matouk, A.R. Conlan, Y. Harir, S. H. Holt, V. Shulaev, M.L. Paddock, A. Hochberg, I.Z. Cabanchick, J.N. Onuchic, P. A. Jennings, R. Nechushtai, R. Mittler, NAF-1 and mitoNEET are central to human breast cancer proliferation by maintaining mitochondrial homeostasis and promoting tumor growth, Proc. Natl. Acad. Sci. U. S. A. 110 (2013) 14676–14681.

[18] M. Darash-Yahana, Y. Pozniak, M. Lu, Y.-S. Sohn, O. Karmi, S. Tamir, F. Bai, L. Song, P.A. Jennings, E. Pikarsky, T. Geiger, J.N. Onuchic, R. Mittler, R. Nechushtai, Breast cancer tumorigenicity is dependent on high expression levels of NAF-1 and the lability of its Fe-S clusters, Proc. Natl. Acad. Sci. 113 (2016) 10890–10895.

[19] B. Chen, S. Shen, J. Wu, Y. Hua, M. Kuang, S. Li, B. Peng, CISD2 associated with proliferation indicates negative prognosis in patients with hepatocellular carcinoma, International Journal of Clinical and Experimental Pathology 8 (2015) 1936–2625.

[20] O.F.L. Wang, X. Liu, S. Wu, H. Wu, Y. Xu, B. Wang, J. Zhu, X. Xu, L. Zhang, Overexpressed CISD2 has prognostic value in human gastric cancer and promotes gastric cancer cell proliferation and tumorigenesis via AKT signaling pathway, Oncotarget 7 (2016) 3791–3805.

[21] Y.-S.B. Yang Yang, Qing Wang, CDGSH Iron sulfur domain 2 activates proliferation and EMT of pancreatic cancer cells via wnt/β-catenin pathway and has prognostic value in human pancreatic cancer, Oncol. Res. 25 (2017) 605–615.

[22] S.-M. Li, C.-H. Chen, Y.-W. Chen, Y.-C. Yen, W.-T. Fang, F.-Y. Tsai, J.-L. Chang, Y.-Y. Shen, S.-F. Huang, C.-P. Chuu, I.S. Chang, C.A. Hsiung, S.S. Jiang, Upregulation of CISD2 augments ROS homeostasis and contributes to tumorigenesis and poor prognosis of lung adenocarcinoma, Sci. Rep. 7 (2017) 11893.

[23] B. Delprat, T. Maurice, C. Delettre, Wolfram syndrome: MAMs' connection? Cell Death Dis. 9 (2018) 364.

[24] C.-H. Wang, Y.-F. Chen, C.-Y. Wu, P.-C. Wu, Y.-L. Huang, C.-H. Kao, C.-H. Lin, L.-S. Kao, T.-F. Tsai, Y.-H. Wei, Cisd2 modulates the differentiation and functioning of adipocytes by regulating intracellular Ca^{2+} homeostasis, Hum. Mol. Genet. 23 (2014) 4770–4785.

[25] N.C. Chang, M. Nguyen, J. Bourdon, P.-A. Risse, J. Martin, G. Danialou, R. Rizzuto, B.J. Petrof, G.C. Shore, Bcl-2-associated autophagy regulator Naf-1 required for maintenance of skeletal muscle, Hum. Mol. Genet. 21 (2012) 2277–2287.

[26] S. Tamir, S. Rotem-Bamberger, C. Katz, F. Morcos, K.L. Hailey, J.A. Zuris, C. Wang, A.R. Conlan, C.H. Lipper, M.L. Paddock, R. Mittler, J.N. Onuchic, P.A. Jennings, A. Friedler, R. Nechushtai, Integrated strategy reveals the protein interface between cancer targets Bcl-2 and NAF-1, Proc. Natl. Acad. Sci. 111 (2014) 5177–5182.

[27] X. Du, R. Xiao, F. Xiao, Y. Chen, F. Hua, S. Yu, G. Xu, NAF-1 antagonizes starvation-induced autophagy through AMPK signaling pathway in cardiomyocytes, Cell Biol. Int. 39 (2015) 816–823.

[28] H. Ivanova, L.E. Wagner, A. Tanimura, E. Vandermarliere, T. Luyten, K. Welkenhuyzen, K.J. Alzayady, L. Wang, K. Hamada, K. Mikoshiba, H. De Smedt, L. Martens, D.I. Yule, J.B. Parys, G. Bultynck, Bcl-2 and IP_3 compete for the ligand-binding domain of IP_3Rs modulating Ca^{2+} signaling output, Cell. Mol. Life Sci. 76 (2019) 3843–3859.

[29] N. Rosa, H. Ivanova, L.E. Wagner, J. Kale, R. La Rovere, K. Welkenhuyzen, N. Louros, S. Karamanou, V. Shabardina, I. Lemmens, E. Vandermarliere, K. Hamada, H. Ando, F. Rousseau, J. Schymkowitz, J. Tavernier, K. Mikoshiba, A. Economou, D.W. Andrews, J.B. Parys, D.I. Yule, G. Bultynck, Bcl-xL acts as an inhibitor of IP_3R channels, thereby antagonizing Ca^{2+}-driven apoptosis, Cell Death & Differentiation 29 (2022) 788–805.

[30] G. Monaco, E. Decrock, H. Akl, R. Ponsaerts, T. Vervliet, T. Luyten, M. De Maeyer, L. Missiaen, C.W. Distelhorst, H. De Smedt, J.B. Parys, L. Leybaert, G. Bultynck, Selective regulation of IP_3-receptor-mediated Ca^{2+} signaling and apoptosis by the BH4 domain of Bcl-2 versus Bcl-xl, Cell Death Differ. 19 (2012) 295–309.

[31] I. de Ridder, M. Kerkhofs, F.O. Lemos, J. Loncke, G. Bultynck, J.B. Parys, The ER-mitochondria interface, where Ca^{2+} and cell death meet, Cell Calcium 112 (2023) 102743.

[32] C. Cauwelier, I. de Ridder, G. Bultynck, Recent advances in canonical versus non-canonical Ca^{2+}-signaling-related anti-apoptotic Bcl-2 functions and prospects for cancer treatment, Biochimica et Biophysica Acta (BBA) - Molecular Cell Research 1871 (2024) 119713.

[33] Y.-P. Rong, A.S. Aromolaran, G. Bultynck, F. Zhong, X. Li, K. McColl, S. Matsuyama, S. Herlitze, H.L. Roderick, M.D. Bootman, G.A. Mignery, J.B. Parys, H. De Smedt, C.W. Distelhorst, Targeting Bcl-2-IP_3 receptor interaction to reverse Bcl-2's inhibition of apoptotic calcium signals, Mol. Cell 31 (2008) 255–265.

[34] P. Duriez, G.M. Shah, Cleavage of poly(ADP-ribose) polymerase: a sensitive parameter to study cell death, Biochem. Cell Biol. 75 (1997) 337–349.

[35] L. Missiaen, K. Van Acker, K. Van Baelen, L. Raeymaekers, F. Wuytack, J.B. Parys, H. De Smedt, J. Vanoevelen, L. Dode, R. Rizzuto, G. Callewaert, Calcium release from the Golgi apparatus and the endoplasmic reticulum in HeLa cells stably expressing targeted aequorin to these compartments, Cell Calcium 36 (2004) 479–487.

[36] G. Monaco, E. Decrock, N. Arbel, A.R. van Vliet, R.M. La Rovere, H. De Smedt, J. B. Parys, P. Agostinis, L. Leybaert, V. Shoshan-Barmatz, G. Bultynck, The BH4 domain of anti-apoptotic Bcl-XL, but not that of the related Bcl-2, limits the voltage-dependent anion channel 1 (VDAC1)-mediated transfer of pro-apoptotic Ca^{2+} signals to mitochondria, J. Biol. Chem. 290 (2015) 9150–9161.

[37] J. Suzuki, K. Kanemaru, K. Ishii, M. Ohkura, Y. Okubo, M. Iino, Imaging intraorganellar Ca^{2+} at subcellular resolution using CEPIA, Nat. Commun. 5 (2014) 4153.

[38] F. Vallese, C. Catoni, D. Cieri, L. Barazzuol, O. Ramirez, V. Calore, M. Bonora, F. Giamogante, P. Pinton, M. Brini, T. Calì, An expanded palette of improved SPLICS reporters detects multiple organelle contacts in vitro and in vivo, Nat. Commun. 11 (2020) 6069.

[39] S. Sakai, S. Watanabe, O. Komine, A. Sobue, K. Yamanaka, Novel reporters of mitochondria-associated membranes (MAM), MAMtrackers, demonstrate MAM disruption as a common pathological feature in amyotrophic lateral sclerosis, FASEB J. 35 (2021) e21688.

[40] D. Cieri, M. Vicario, M. Giacomello, F. Vallese, R. Filadi, T. Wagner, T. Pozzan, P. Pizzo, L. Scorrano, M. Brini, T. Calì, SPLICS: a split green fluorescent protein-based contact site sensor for narrow and wide heterotypic organelle juxtaposition, Cell Death & Differentiation 25 (2018) 1131–1145.

[41] M.A. Carpio, R.E. Means, A.L. Brill, A. Sainz, B.E. Ehrlich, S.G. Katz, BOK controls apoptosis by Ca^{2+} transfer through ER-mitochondrial contact sites, Cell Rep. 34 (2021) 108827.

[42] B. Bonneau, H. Ando, K. Kawaai, M. Hirose, H. Takahashi-Iwanaga, K. Mikoshiba, IRBIT controls apoptosis by interacting with the Bcl-2 homolog, Bcl2l10, and by promoting ER-mitochondria contact, eLife 5 (2016) e19896.

[43] S. Pattingre, A. Tassa, X. Qu, R. Garuti, X.H. Liang, N. Mizushima, M. Packer, M. D. Schneider, B. Levine, Bcl-2 Antiapoptotic proteins inhibit Beclin 1-dependent autophagy, Cell 122 (2005) 927–939.

[44] L. Crouzier, A. Danese, Y. Yasui, E.M. Richard, J.-C. Liévens, S. Patergnani, S. Couly, C. Diez, M. Denus, N. Cubedo, M. Rossel, M. Thiry, T.-P. Su, P. Pinton, T. Maurice, B. Delprat, Activation of the sigma-1 receptor chaperone alleviates symptoms of Wolfram syndrome in preclinical models, Science Translational Medicine, 14 eabh3763.

[45] M. Liiv, A. Vaarmann, D. Safiulina, V. Choubey, R. Gupta, M. Kuum, L. Janickova, Z. Hodurova, M. Cagalinec, A. Zeb, M.A. Hickey, Y.-L. Huang, N. Gogichaishvili, M. Mandel, M. Plaas, E. Vasar, J. Loncke, T. Vervliet, T.-F. Tsai, G. Bultynck, V. Veksler, A. Kaasik, ER calcium depletion as a key driver for impaired ER-to-mitochondria calcium transfer and mitochondrial dysfunction in Wolfram syndrome, Nat. Commun. 15 (2024) 6143.

[46] J.B. Parys, H. De Smedt, L. Missiaen, M.D. Bootman, I. Sienaert, R. Casteels, Rat basophiliv leukemia cells as model system for inositol 1,4,5-trisphosphate receptor IV, a receptor of the type II family: functional comparison and immunological detection, Cell Calcium 17 (1995) 239–249.

[47] T. Vervloessem, B.K. Sasi, E. Xerxa, S. Karamanou, J. Kale, R.M. La Rovere, S. Chakraborty, F. Sneyers, M. Vogler, A. Economou, L. Laurenti, D.W. Andrews, D. G. Efremov, G. Bultynck, BDA-366, a putative Bcl-2 BH4 domain antagonist, induces apoptosis independently of Bcl-2 in a variety of cancer cell models, Cell Death Dis. 11 (2020) 769.

[48] T. Vervliet, I. Lemmens, E. Vandermarliere, E. Decrock, H. Ivanova, G. Monaco, V. Sorrentino, N.N. Kasri, L. Missiaen, L. Martens, H. De Smedt, L. Leybaert, J. B. Parys, J. Tavernier, G. Bultynck, Ryanodine receptors are targeted by anti-apoptotic Bcl-XL involving its BH4 domain and Lys87 from its BH3 domain, Sci. Rep. 5 (2015) 9641.
[49] T. Vervliet, I. Lemmens, K. Welkenhuyzen, J. Tavernier, J.B. Parys, G. Bultynck, Regulation of the ryanodine receptor by anti-apoptotic Bcl-2 is independent of its BH3-domain-binding properties, Biochem. Biophys. Res. Commun. 463 (2015) 174–179.
[50] F.A. Ran, P.D. Hsu, J. Wright, V. Agarwala, D.A. Scott, F. Zhang, Genome engineering using the CRISPR-Cas9 system, Nat. Protoc. 8 (2013) 2281–2308.
[51] T. Luyten, K. Welkenhuyzen, G. Roest, E. Kania, L. Wang, M. Bittremieux, D.I. Yule, J.B. Parys, G. Bultynck, Resveratrol-induced autophagy is dependent on IP_3Rs and on cytosolic Ca^{2+}, Biochimica et Biophysica Acta (BBA) - Molecular Cell Research 1864 (2017) 947–956.
[52] F.O. Lemos, I. de Ridder, L. Wagner, M.D. Bootman, G. Bultynck, D.I. Yule, J. B. Parys, Tetrameric, active PKM2 inhibits IP_3 receptors, potentially requiring GRP75 as an additional interaction partner, Biochimica et Biophysica Acta (BBA) - Molecular Cell Research 1871 (2024) 119796.
[53] L.E. Wagner Ii, D.I. Yule, Differential regulation of the IP_3 receptor type-1 and -2 single channel properties by IP_3, Ca^{2+} and ATP, J. Physiol. 590 (2012) 3245–3259.
[54] M.R. Wieckowski, C. Giorgi, M. Lebiedzinska, J. Duszynski, P. Pinton, Isolation of mitochondria-associated membranes and mitochondria from animal tissues and cells, Nat. Protoc. 4 (2009) 1582–1590.
[55] J. Schindelin, I. Arganda-Carreras, E. Frise, V. Kaynig, M. Longair, T. Pietzsch, S. Preibisch, C. Rueden, S. Saalfeld, B. Schmid, J.-Y. Tinevez, D.J. White, V. Hartenstein, K. Eliceiri, P. Tomancak, A. Cardona, Fiji: an open-source platform for biological-image analysis, Nat. Methods 9 (2012) 676–682.
[56] H. Wickham, ggplot2: Elegant Graphics for Data Analysis, Springer-Verlag, Place Published, 2016.
[57] R.C. Team, R: A Language and Environment for Statistical Computing, R Foundation for Statistical Computing, Vienna, Austria, 2021.
[58] C. Ritz, F. Baty, J.C. Streibig, D. Gerhard, Dose-response analysis using R, PloS One 10 (2016) e0146021.
[59] S.W. John Fox, An R Companion to Applied Regression, Sage, Thousand Oaks CA, 2019.
[60] C.R. Harris, K.J. Millman, S.J. van der Walt, R. Gommers, P. Virtanen, D. Cournapeau, E. Wieser, J. Taylor, S. Berg, N.J. Smith, R. Kern, M. Picus, S. Hoyer, M.H. van Kerkwijk, M. Brett, A. Haldane, J.F. del Río, M. Wiebe, P. Peterson, P. Gérard-Marchant, K. Sheppard, T. Reddy, W. Weckesser, H. Abbasi, C. Gohlke, T.E. Oliphant, Array programming with NumPy, Nature 585 (2020) 357–362.
[61] W. McKinney, Data Structures for Statistical Computing in Python Place Published, 2010.